Tribology International 171 (2022) 107570

Contents lists available at ScienceDirect

Tribology International

journal homepage: www.elsevier.com/locate/triboint

Structural design for planetary roller screw mechanism based on the developed contact modelling

Qin Yao [a,*], Mengchuang Zhang [b,c,**], Shangjun Ma [d]

[a] School of Mechanical Engineering, Suzhou University of Science and Technology, Su Zhou 215009, PR China
[b] School of Civil Aviation, Northwestern Polytechnical University, Xi'an 710072, PR China
[c] Yangtze River Delta Research Institute of NPU, Taicang City 215400, PR China
[d] Shaanxi Engineering Laboratory for Transmissions and Controls, Northwestern Polytechnical University, Xi'an 710072, PR China

ARTICLE INFO

Keywords:
Planetary roller screw mechanism
Structural design
Contact characteristics
Multi-objective optimization

ABSTRACT

The structural design of planetary roller screw mechanism (PRSM) with lower contact stress is beneficial to delay the fatigue failure and prolong the service life. However, few studies focused on this field and a reasonable contact model is therefore required due to its complexity structure. In this paper, a developed contact model is established for PRSM, and a process-based parameterization method is proposed to precisely calculate the contact characteristics along with the change of parameters. Based on the in-depth study of the parameter sensitivities of contact characteristics, the structure design to reduce contact stress for PRSM is realized through the multi-objective optimization under the proposed geometric constraints. The validity of this model is well verified by finite element method.

1. Introduction

Planetary roller screw mechanism (PRSM) is one of the key actuators in electromechanical servo system [1], and is widely used in military and civil fields such as aircraft [2], radio telescope [3], robot [4] and food processing [5]. As a precision mechanical transmission device, the PRSM can transfer the motion and force through a series of rollers making planetary motions between the nut and the screw. The multi-body and multi-point contacts therefore contribute to a high load carrying capacity of the PRSM. Meanwhile, each contact point expands into an elliptical region after loading, and the shape and size of which will then affect the properties of friction and lubrication [6,7], and further affect the transmission efficiency [8] and thermal characteristics [9]. Besides, a large stress can be generated even under a slight load since the area of the contact ellipse is small enough. The stress distribution in this region, especially the maximum stress, has an important impact on the fatigue wear [10] and plastic deformation [11], which considerably determines the service life of PRSM [12]. In addition, the nonlinearity of contact deformation will contribute to the non-uniform load distribution among threads by affecting the structural stiffness of PRSM [13]. Furthermore, the contact positions are also closely related to the clearances of mating thread surfaces [14,15], the kinematics [16,17] and dynamics [18]. Therefore, the contact characteristics analysis of PRSM is the foundation for the above studies.

In recent years, many beneficial methods and conclusions have been presented by scholars. The classical method to study the contact characteristics is based on Hertz contact theory, and the key is to obtain the principal curvatures at the contact point of two objects. The contact position can be ignored by treating each thread tooth of the roller as an equivalent ball with approximate principal curvatures, and this method has been widely used in many literatures [6–9,11–13]. However, the application of differential geometry theory enables a more accurate study at the actual contact point considering thread profile features. Jones et al. [19] established the contact model in PRSM based on the principle of conjugate surfaces, and analyzed the influence of some parameters on the curvature radii, contact stress and deformation. Sandu et al. studied the thread contact geometry and surface assembly in PRSM [20], and deduced some contact characteristics based on differential geometry theory and Hertz theory [16]. Similarly, based on the above two theories, Ma et al. investigated the local contact characteristics [21] and the static contact with friction [22] of PRSM, and conducted sensitivity analysis of various structural parameters. In addition, the contact characteristics of PRSM can be studied based on fractal theory [4], and the finite element method (FEM) is also a common way of analysis and verification [21–23].

* Corresponding author.
** Corresponding author at: School of Civil Aviation, Northwestern Polytechnical University, Xi'an 710072, PR China.
E-mail addresses: yaoqin@usts.edu.cn (Q. Yao), mczhang@nwpu.edu.cn (M. Zhang).

https://doi.org/10.1016/j.triboint.2022.107570
Received 1 February 2022; Received in revised form 22 March 2022; Accepted 30 March 2022
Available online 3 April 2022
0301-679X/

Nomenclature

S, N, R denote the screw, nut, roller
$*$ S, N, denotes the screw-roller or nut-roller interface
$\mathcal{T}$ circular helix
$\boldsymbol{\Sigma}_u, \boldsymbol{\Sigma}_l$ upper and lower contact surface of the thread
(r, α) polar coordinate of the projection of a point
r_{Sc}, α_{Sc} contact radius and deflection angle of screw
r_{RSc}, α_{RSc} contact radius and deflection angle of roller on screw-roller interface
r_{Nc}, α_{Nc} contact radius and deflection angle of nut
r_{RNc}, α_{RNc} contact radius and deflection angle of roller on nut-roller interface
r_e radius of the arc thread profile of the roller
$\boldsymbol{\Omega}$ primary area
$\boldsymbol{\epsilon}$ plane determined by a point and z-axis
l lead of the thread
$\boldsymbol{\psi}(r, \alpha)$ parametric equation of the space helical surface
$\boldsymbol{\psi}_r, \boldsymbol{\psi}_\alpha$ the first partial derivative of $\boldsymbol{\psi}(r, a)$
$\boldsymbol{\psi}_{rr}, \boldsymbol{\psi}_{r\alpha}, \boldsymbol{\psi}_{\alpha\alpha}$ the second partial derivative of $\boldsymbol{\psi}(r, a)$
$\phi(r)$ thread profile function
$\phi'(r)$ the first derivative of $\phi(r)$
$\phi''(r)$ the second derivative of $\phi(r)$
$\boldsymbol{N}, \boldsymbol{n}$ normal vector and unit normal vector of the surface
κ_n normal curvature
E, F, G the first fundamental form of a general parametric surface
L, M, N the second fundamental form of a general parametric surface
$\boldsymbol{e}_1, \boldsymbol{e}_2$ the first and second principal directions
$\boldsymbol{e}_{*1}, \boldsymbol{e}_{*2}$ the first and second principal directions of the screw or nut
$\boldsymbol{e}_{R*1}, \boldsymbol{e}_{R*2}$ the first and second principal directions of the roller
κ_1, κ_2 the first and second principal curvatures
κ_{*1}, κ_{*2} the first and second principal curvatures of the screw or nut
$\kappa_{R*1}, \kappa_{R*2}$ the first and second principal curvatures of the roller
$\boldsymbol{n}_{Sc}, \boldsymbol{n}_{RSc}$ unit normal vectors at the contact point of screw and roller
$\boldsymbol{N}_{Nc}, \boldsymbol{n}_{RNc}$ unit normal vectors at the contact point of nut and roller
$\zeta = 1, \zeta = -1$ Boolean variable, represents the lower and upper helical surface of thread
ζ_{Sc}, ζ_{RSc} the contact helical surfaces of the screw and roller
ζ_{Nc}, ζ_{RNc} the contact helical surfaces of the nut and roller
λ_R helix angle of roller
$Q_{*R}, F_{*R}, F_{*Rt}, F_{*Rr}$ normal force, axial force, tangential force and radial force
γ_{R*} angle between the first principal planes of the contact surfaces
γ_1, γ_2 angle between x-axis and x_{R*}-axis, angle between x-axis and x_*-axis
$f(\kappa)$ function of principal curvatures
$\Sigma\kappa$ curvature sum
A, B coefficient
$K(e), L(e)$ complete elliptic integrals of the first and second kinds
a, b semimajor and semiminor axes of the contact ellipse
k_e the ratio of b to a
e eccentricity of the contact ellipse
E' equivalent elastic modulus
δ_H, σ_H contact deformation, contact stress
$\boldsymbol{\beta} = (\beta_S, \beta_R, \beta_N)$ design variables
$\boldsymbol{\beta}^l, \boldsymbol{\beta}^u$ lower and upper limit of the design space
$\mathbf{C_X}$ design constants
$\sigma_{HSR} = g_{SR}(\boldsymbol{\beta}, \mathbf{C_X})$ objective function of the contact stress between screw and roller
$\sigma_{HNR} = g_{NR}(\boldsymbol{\beta}, \mathbf{C_X})$ objective function of the contact stress between nut and roller
a_S, a_R, a_N root widths of screw, roller and nut
c_S, c_R, c_N crest widths of screw, roller and nut
$\varepsilon_{SRc}, \varepsilon_{NRc}$ axial clearance between the thread surfaces to be contacted
$\varepsilon_{ST}, \varepsilon_{NT}$ axial clearance from the thread crown of screw or nut to the corresponding helical surface of roller
$\varepsilon_{RST}, \varepsilon_{RNT}$, axial clearance from the thread crown of roller to the corresponding helical surface of screw or nut
h_{aS}, h_{aR}, h_{aN} thread addendum of screw, roller and nut

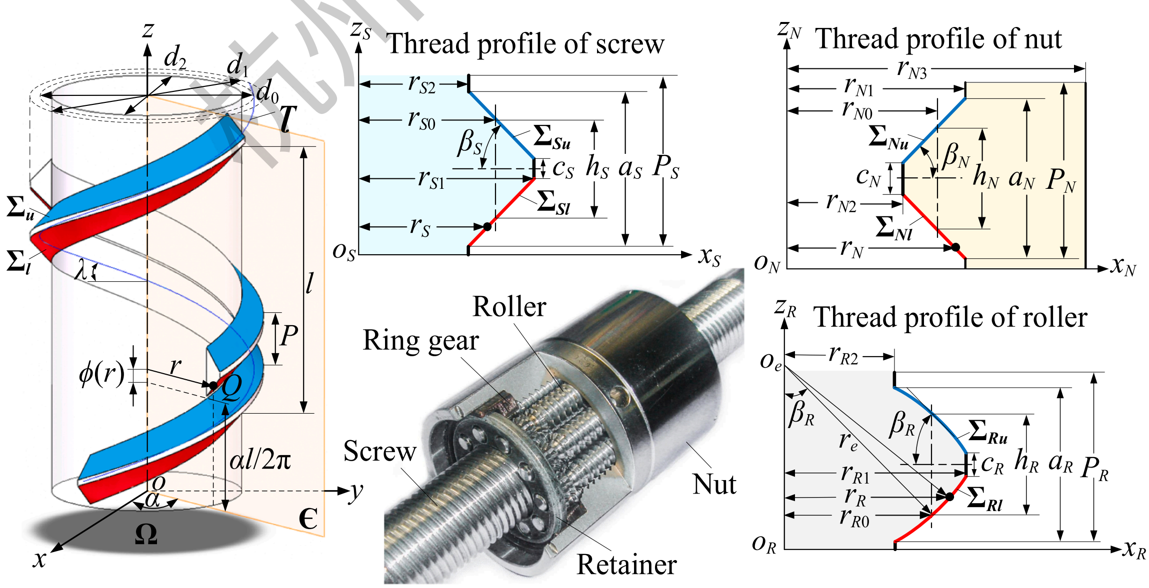

Fig. 1. Structural diagram and independent part coordinate systems of PRSM.

These studies have promoted the development of PRSM, but there are still some problems to be improved. Some literatures used complex coordinate systems with tedious coordinate transformations, which increased computational costs but the contact characteristics did not change with the choice of coordinate systems. Also, the existing literatures mainly studied the sensitivity of parameters through mono-factor analysis, namely, a specific parameter changes within a given and usually large range while keeping other parameters constant. However, this method ignores the interaction and restriction between the parameters of the actual product. Furthermore, threads are the most vulnerable parts of the PRSM [5,11], but few improvements have been reported. Therefore, this paper focuses on the structural design of the thread profiles through multi-objective optimization, so as to pursue lower contact stress on the screw-roller and nut-roller interfaces simultaneously, which is of great significance for slowing down fatigue failure, preventing plastic deformation and prolonging the service life of PRSM. The structure of this paper are as follows:

Firstly, in Section 2, the developed contact model of PRSM is established by using the independent coordinate systems of screw, roller and nut without coordinate transformation. Based on the differential geometry theory, continuous tangency conditions and Hertz contact theory, the contact characteristics of PRSM are deeply studied in a parameterized and process-based way. The principal curvatures and directions, local contact geometry and contact parameters at the exact contact position are calculated in detail. Then, in Section 3, the parameter sensitivities on the contact characteristics are comprehensively revealed by the design of experiments (DOE). Subsequently, the structural parameters most sensitive to contact stress are selected as design variables, and multi-objective optimization under the proposed geometric constraints is further conducted to obtain the optimal structural design. Next, the optimization results verified by FEM are discussed in Section 4. Finally, Section 5 presented the main conclusions of this paper.

2. Theory and methodology

2.1. Parametric equation

The PRSM consists of a screw, a nut, multiple rollers, two ring gears and two retainers. The threads of screw, roller and nut are the main load bearing parts and can be regarded as the continuous convex or concave structure formed by a specific profile along the circular helix $\mathcal{T}$. Therefore, the thread surface can be divided into upper and lower spatial helical surfaces, as shown in Fig. 1, where the blue one represents the upper contact surface of the thread and is denoted by symbol $\boldsymbol{\Sigma_u}$, while the red one represents the lower contact surface of the thread and is denoted by symbol $\boldsymbol{\Sigma_l}$.

By establishing the Cartesian coordinate system o-xyz, the position of an arbitrary point Q on the thread can be accurately described, in which the z-axis is on the axis of the corresponding part, and the upper and lower profiles are symmetrical about the x axis to distinguish the helical surface $\boldsymbol{\Sigma_u}$ and $\boldsymbol{\Sigma_l}$. Then, the Q is not only on the helical surface, but also on the plane $\boldsymbol{\epsilon}$ determined by Q and z-axis, and its coordinates are (x, y, z). If the angle between the plane xoz and $\boldsymbol{\epsilon}$ is α, and the distance from Q to the z-axis is r, then the polar coordinate of the projection of Q is (r, α) on a primary area $\boldsymbol{\Omega}$ of plane xoy, *i.e.*, the helical surface $\boldsymbol{\Sigma_u}$ or $\boldsymbol{\Sigma_l}$ can be obtained by mapping from $\boldsymbol{\Omega}$. Therefore, the parametric equation of an arbitrary point on the spatial helical surface can be expressed as

$$\begin{cases} x = r\cos\alpha \\ y = r\sin\alpha \\ z = \zeta\phi(r) + \alpha l/(2\pi) \end{cases} \quad (r,\alpha)\in\boldsymbol{\Omega} \tag{1}$$

where ζ is a Boolean variable, $\zeta = 1$ represents lower helical surface of thread, whereas $\zeta = -1$ represents the upper one. $\phi(r)$ is the function of thread profile determined only by the parameter r, specifying that $\phi(r)>$ 0 in its domain of definition $d_2/2 \le r \le d_1/2$, where d_1 and d_2 refer to the major and minor diameter of the thread. Besides, d_0, P and l are the nominal diameter, pitch and lead, respectively. And $l=np$, n is the starts of the thread.

In general, the screw and nut are external and internal trapezoidal multi-start threads with equal number of starts. The roller is a single-start external thread with a convex arc profile. Then three independent coordinate systems of the screw, nut and roller are established based on their thread characteristics, as shown in Fig. 1, which can effectively avoid complex coordinate transformation in the subsequent calculation process. It should be noted that the subscripts $_S$, $_N$ and $_R$ denote the screw, nut and roller throughout this paper, respectively. Accordingly, the thread profile function of screw and nut, *i.e.*, $\phi_S(r_S)$ and $\phi_N(r_N)$ can be deduced as

$$\phi_S(r_S) = (r_S - d_{S0}/2)\tan\beta_S + (P_S - h_S)/2 \quad (d_{S2}/2 \le r_S \le d_{S1}/2) \tag{2}$$

$$\phi_N(r_N) = (P_N - h_N)/2 - (r_N - d_{N0}/2)\tan\beta_N \quad (d_{N2}/2 \le r_N \le d_{N1}/2) \tag{3}$$

Where d_{*0}, d_{*1}, d_{*2}, h_*, β_* and r_* ($*=_S$, $_N$) are the nominal diameter, major diameter, minor diameter, thread thickness, flank angle and the position parameter of the point on the thread profile of the screw or the nut. In Fig. 1, r_{*0}, r_{*1} and r_{*2} correspond in turn to the radii of d_{*0}, d_{*1} and d_{*2}, and r_{N3} is radii at the external diameter d_{N3} of the nut. Similarly, the parameters described above are denoted by subscript $_R$ for the roller. When the center o_e of the arc thread profile is located on the axis of the roller, its radius can be deduced as $r_e=d_{R0}/2\sin\beta_R$, and the thread profile function $\phi_R(r_R)$ is

$$\phi_R(r_R) = r_e\cos\beta_R + (P_R - h_R)/2 - \sqrt{r_e^{\,2} - r_R^{\,2}} \quad (d_{R2}/2 \le r_R \le d_{R1}/2) \tag{4}$$

2.2. Local contact characteristics

2.2.1. Principal curvatures and directions

The contact between the threads of roller and screw (nut) is actually the contact between two spatial helical surfaces with different principal curvatures. Therefore, the principal curvatures are critical for studying the contact characteristics.

Firstly, the parametric equation Eq.(1) of the space helical surface can be expressed in vector form as $\boldsymbol{\psi}(r, \alpha)$= [$rcos\alpha$, $r$sinα, $\zeta\phi(r)$+αl/(2π)]. Then, for parameters r and α of the helical surface Σ: $\boldsymbol{\psi} = \boldsymbol{\psi}(r, \alpha)$, ($r$, α)∈$\boldsymbol{\Omega}$, the partial derivatives of the first order $\boldsymbol{\psi}_r$ and $\boldsymbol{\psi}_\alpha$ and the second order $\boldsymbol{\psi}_{rr}$, $\boldsymbol{\psi}_{r\alpha}$ and $\boldsymbol{\psi}_{\alpha\alpha}$ can be derived as

$$\begin{cases} \boldsymbol{\psi}_r = \dfrac{\partial\boldsymbol{\psi}}{\partial r} = [\cos\alpha,\ \sin\alpha, \zeta\phi'(r)] \\ \boldsymbol{\psi}_\alpha = \dfrac{\partial\boldsymbol{\psi}}{\partial\alpha} = [-r\sin\alpha, r\cos\alpha, l/(2\pi)] \end{cases} \tag{5}$$

$$\begin{cases} \boldsymbol{\psi}_{rr} = \dfrac{\partial^2\boldsymbol{\psi}}{\partial r^2} = [0, 0, \zeta\phi''(r)] \\ \boldsymbol{\psi}_{r\alpha} = \dfrac{\partial^2\boldsymbol{\psi}}{\partial r\partial\alpha} = [-\ \sin\alpha,\ \cos\alpha, 0] \\ \boldsymbol{\psi}_{\alpha\alpha} = \dfrac{\partial^2\boldsymbol{\psi}}{\partial\alpha^2} = [-r\cos\alpha, -r\sin\alpha, 0] \end{cases} \tag{6}$$

Where $\phi'(r)$ and $\phi''(r)$ are the first and second derivatives of thread profile function to the parameter r, respectively. These two expressions for the screw, nut and roller can be obtained from Eq.(2)~Eq.(4), namely:

$$\begin{cases} \phi_S{'}(r_S) = \tan\beta_S \\ \phi_S{''}(r_S) = 0 \end{cases} \tag{7}$$

$$\begin{cases} \phi_N{'}(r_N) = -\tan\beta_N \\ \phi_N{''}(r_N) = 0 \end{cases} \tag{8}$$

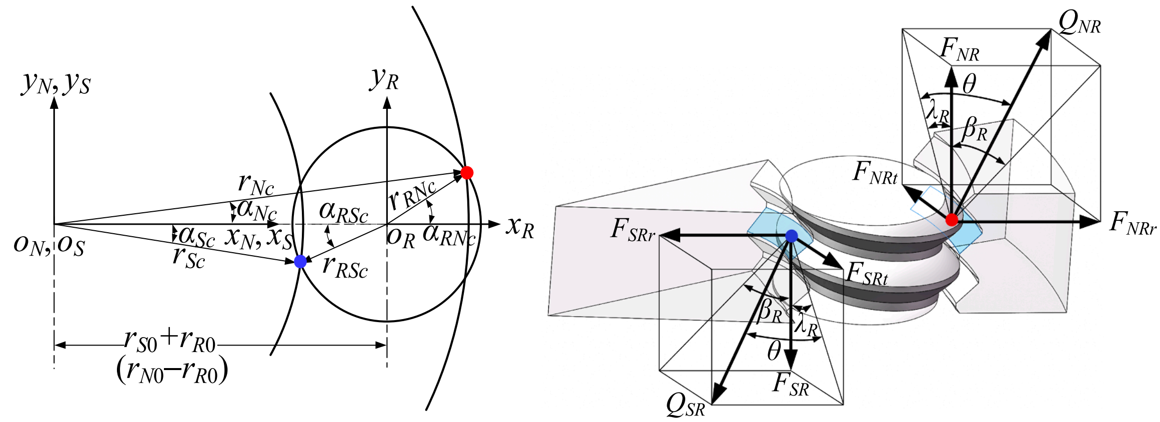

Fig. 2. Static force analysis at contact points.

$$\begin{cases} \phi_R{}'(r_R) = r_R\cdot\left(r_e{}^2 - r_R{}^2\right)^{-1/2} \\ \phi_R{}''(r_R) = \left(r_e{}^2 - r_R{}^2\right)^{-1/2} + r_R{}^2\cdot\left(r_e{}^2 - r_R{}^2\right)^{-3/2} \end{cases} \tag{9}$$

Besides, if $\boldsymbol{\psi}_r \times \boldsymbol{\psi}_\alpha \neq 0$ at an arbitrary point on the helical surface Σ: $\boldsymbol{\psi} = \boldsymbol{\psi}(r, \alpha)$, $(r, \alpha)\in\boldsymbol{\Omega}$, the normal vector $\boldsymbol{N}$ of the surface at that point can be represented by $\boldsymbol{\psi}_r \times \boldsymbol{\psi}_\alpha$. However, in order to avoid the change of contact characteristics caused by different choices of upper or lower helical surfaces, it is necessary to uniformly specify that the normal direction points to the inside of the thread teeth, namely, the normal vector $\boldsymbol{N}$ is defined as

$$\begin{aligned} N &= \zeta\boldsymbol{\psi}_r \times \boldsymbol{\psi}_\alpha \\ &= [\zeta l \sin\alpha/(2\pi) - r\cos\alpha\phi'(r),\ -\zeta l\cos\alpha/(2\pi) - r\sin\alpha\phi'(r), \zeta r] \end{aligned} \tag{10}$$

Further, the unit normal vector can be expressed as $\boldsymbol{n}=\boldsymbol{N}/|\boldsymbol{N}|$, then that of screw, nut and roller can be deduced accordingly as

$$\boldsymbol{n}_S = \zeta_S\left\{1 + [l_S/(2\pi r_S)]^2 + \tan^2\beta_S\right\}^{-1/2}\cdot\begin{bmatrix} l_S\sin\alpha_S/(2\pi r_S) - \zeta_S\cos\alpha_S\tan\beta_S \\ -l_S\cos\alpha_S/(2\pi r_S) - \zeta_S\sin\alpha_S\tan\beta_S \\ 1 \end{bmatrix}^T \tag{11}$$

$$\boldsymbol{n}_N = \zeta_N\left\{1 + [l_N/(2\pi r_N)]^2 + \tan^2\beta_N\right\}^{-1/2}\cdot\begin{bmatrix} l_N\sin\alpha_N/2\pi r_N + \zeta_N\cos\alpha_N\tan\beta_N \\ -l_N\cos\alpha_N/2\pi r_N + \zeta_N\sin\alpha_N\tan\beta_N \\ 1 \end{bmatrix}^T \tag{12}$$

$$\boldsymbol{n}_R = \zeta_R\left[1 + \left(\frac{l_R}{2\pi r_R}\right)^2 + \frac{r_R{}^2}{r_e{}^2 - r_R{}^2}\right]^{-1/2}\cdot\begin{bmatrix} \dfrac{l_R\sin\alpha_R}{2\pi r_R} - \dfrac{\zeta_R\cos\alpha_R r_R}{\sqrt{r_e{}^2 - r_R{}^2}} \\ -\dfrac{l_R\cos\alpha_R}{2\pi r_R} - \dfrac{\zeta_R\sin\alpha_R r_R}{\sqrt{r_e{}^2 - r_R{}^2}} \\ 1 \end{bmatrix}^T \tag{13}$$

Based on the differential geometry theory [24], the normal curvature κ_n of an arbitrary point on the surface Σ: $\boldsymbol{\psi} = \boldsymbol{\psi}(r, \alpha)$, $(r, \alpha)\in\boldsymbol{\Omega}$ along the direction (d)=dr:dα at that point is

$$\kappa_n = \frac{II}{I} = \frac{d^2\boldsymbol{\psi}\cdot\boldsymbol{n}}{d\boldsymbol{\psi}^2} = \frac{Ldr^2 + 2Mdrd\alpha + Nd\alpha^2}{Edr^2 + 2Fdrd\alpha + Gd\alpha^2} \tag{14}$$

where I and II are the first and second fundamental form of a general parametric surface, and the coefficients are given by

$$\begin{cases} E = \boldsymbol{\psi}_r\cdot\boldsymbol{\psi}_r = 1 + [\phi'(r)]^2 \\ F = \boldsymbol{\psi}_r\cdot\boldsymbol{\psi}_\alpha = \zeta l\phi'(r)/(2\pi) \\ G = \boldsymbol{\psi}_\alpha\cdot\boldsymbol{\psi}_\alpha = r^2 + [l/(2\pi)]^2 \end{cases} \tag{15}$$

$$\begin{cases} L = \boldsymbol{\psi}_{rr}\cdot\boldsymbol{n} = r\phi''(r)\cdot\left\{r^2 + [l/(2\pi)]^2 + [r\phi'(r)]^2\right\}^{-1/2} \\ M = \boldsymbol{\psi}_{r\alpha}\cdot\boldsymbol{n} = -\zeta l/(2\pi)\cdot\left\{r^2 + [l/(2\pi)]^2 + [r\phi'(r)]^2\right\}^{-1/2} \\ N = \boldsymbol{\psi}_{\alpha\alpha}\cdot\boldsymbol{n} = r^2\phi'(r)\cdot\left\{r^2 + [l/(2\pi)]^2 + [r\phi'(r)]^2\right\}^{-1/2} \end{cases} \tag{16}$$

The principal curvatures κ_1 and κ_2 are the maximum and minimum of the normal curvature at a given point on the surface, and satisfy the following relationship

$$K = \kappa_1\cdot\kappa_2 = \left(LN - M^2\right)/\left(EG - F^2\right) \tag{17}$$

$$H = (\kappa_1 + \kappa_2)/2 = (LG - 2MF + NE)/\left(2EG - 2F^2\right) \tag{18}$$

where K and H represent the Gauss curvature and mean curvature respectively. The shape of the surface near this point is convex when $K > 0$, and its shape is approximately saddle surface when $K < 0$. Furthermore, κ_1 and κ_2 can be expressed by K and H as

$$\kappa_1, \kappa_2 = H \pm \sqrt{H^2 - K} \tag{19}$$

The directions corresponding to the principal curvatures κ_1 and κ_2 are the two principal directions of the surface at this point, which are both orthogonal and conjugate. On this basis, the unit direction vectors $\boldsymbol{e}_1$ and $\boldsymbol{e}_2$ of the first and second principal directions can be deduced as

$$\boldsymbol{e}_1, \boldsymbol{e}_2 = \frac{\boldsymbol{\psi}_r\frac{dr}{d\alpha} + \boldsymbol{\psi}_\alpha}{\left|\boldsymbol{\psi}_r\frac{dr}{d\alpha} + \boldsymbol{\psi}_\alpha\right|} \tag{20}$$

Except for $F/L=F/M=G/N$, there is:

$$\frac{dr}{d\alpha} = \frac{-\left(EN - GL\right) \pm \sqrt{\left(EN - GL\right)^2 - 4\left(EM - FL\right)\left(FN - GM\right)}}{2(EM - FL)} \tag{21}$$

The unit direction vectors $\boldsymbol{e}_1$, $\boldsymbol{e}_2$ and the unit normal vector $\boldsymbol{n}$ will form a standard orthonormal basis at any point of the surface. The planes determined by $\boldsymbol{e}_1$, $\boldsymbol{e}_2$ and $\boldsymbol{n}$ are called the first and second principal planes, and the principal curvatures of the normal section of the surface on these two planes are κ_1 and κ_2 respectively. To avoid confusion, it is specified $|\kappa_1| < |\kappa_2|$ in this paper, *i.e.*, the first principal direction is defined as the direction with small absolute value of curvature, and *vice versa* is the second principal direction. Moreover, the principal curvatures and directions of the surface at a point are exactly the eigenvalues and eigenvectors of the Weingarten transformation at that point. Where, Weingarten matrix is:

$$W = \begin{bmatrix} L & M \\ M & N \end{bmatrix}\begin{bmatrix} E & F \\ F & G \end{bmatrix}^{-1} \tag{22}$$

Then the principal curvatures and principal directions can be

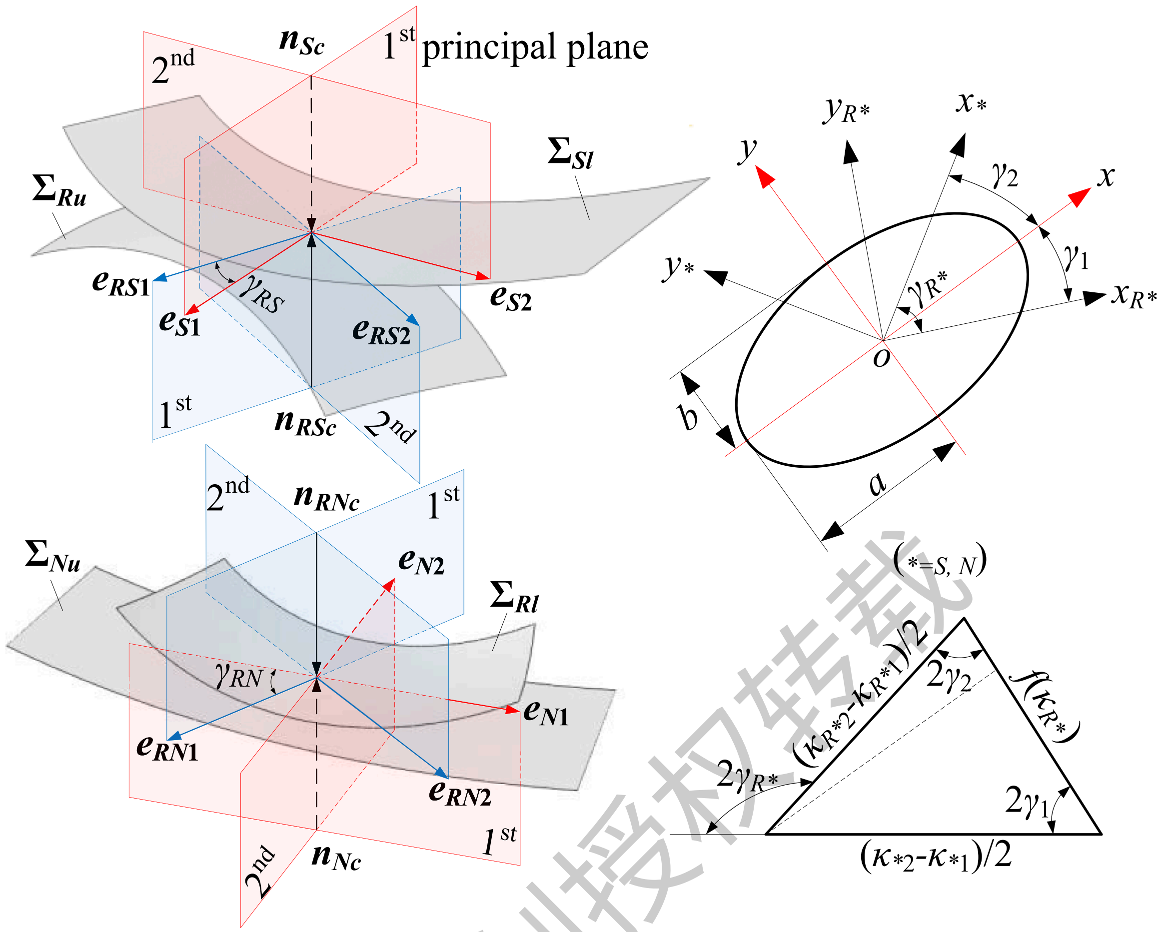

Fig. 3. Local contact geometry.

deduced as

$$\begin{bmatrix}\kappa_1 & 0\\ 0 & \kappa_2\end{bmatrix} = \begin{bmatrix} e_{11} & e_{12}\\ e_{21} & e_{22}\end{bmatrix}^{-1} W \begin{bmatrix} e_{11} & e_{12}\\ e_{21} & e_{22}\end{bmatrix} \tag{23}$$

$$\boldsymbol{e}_1 = \frac{e_{11}\boldsymbol{\Psi}_r + e_{21}\boldsymbol{\Psi}_\alpha}{|e_{11}\boldsymbol{\Psi}_r + e_{21}\boldsymbol{\Psi}_\alpha|} \ \textit{and}\ \boldsymbol{e}_2 = \frac{e_{12}\boldsymbol{\Psi}_r + e_{22}\boldsymbol{\Psi}_\alpha}{|e_{12}\boldsymbol{\Psi}_r + e_{22}\boldsymbol{\Psi}_\alpha|} \tag{24}$$

In this way, κ_1, κ_2, $\boldsymbol{e}_1$ and $\boldsymbol{e}_2$ can be calculated more effectively based on the programming language.

2.2.2. *Contact position*

Based on the calculation of principal curvatures at an arbitrary point on the helical surface, the precise contact positions on screw-roller and nut-roller interfaces are particularly important for the study of contact characteristics. Therefore, the static force analysis is performed at the contact points of PRSM with single thread pairs on both sides of roller, as shown in Fig. 2.

On the screw-roller interface, the contact radius and deflection angle of screw are r_{Sc} and α_{Sc}, and those of roller are r_{RSc} and α_{RSc}, respectively. Therefore, the parametric coordinates of the contact point on the $x_So_Sy_S$ plane of the screw are (r_{Sc}, α_{Sc}), and that on the $x_Ro_Ry_R$ plane of the roller are (r_{RSc}, π-α_{RSc}). Based on the continuous tangency condition [14], the unit normal vectors of the two mating surfaces should be collinear, *i.e.*, $\boldsymbol{n}_{Sc}$= -$\boldsymbol{n}_{RSc}$. Combining Eq.(11), Eq.(13) and the installation position of screw and roller, the quaternion equation is given as

$$\begin{cases} \dfrac{l_S\sin\alpha_{Sc}}{2\pi r_{Sc}} - \zeta_{Sc}\cos\alpha_{Sc}\tan\beta_S = \dfrac{l_R\sin(\pi-\alpha_{RSc})}{2\pi r_{RSc}} - \dfrac{\zeta_{RSc} r_{RSc}\cos(\pi-\alpha_{RSc})}{\sqrt{r_e^{\,2}-r_{RSc}^{\,2}}} \\ -\dfrac{l_S\cos\alpha_{Sc}}{2\pi r_{Sc}} - \zeta_{Sc}\sin\alpha_{Sc}\tan\beta_S = -\dfrac{l_R\cos(\pi-\alpha_{RSc})}{2\pi r_{RSc}} - \dfrac{\zeta_{Rc} r_{RSc}\sin(\pi-\alpha_{RSc})}{\sqrt{r_e^{\,2}-r_{RSc}^{\,2}}} \\ r_{Sc}\sin\alpha_{Sc} = r_{RSc}\sin\alpha_{RSc} \\ r_{Sc}\cos\alpha_{Sc} + r_{RSc}\cos\alpha_{RSc} = (d_{S0}+d_{R0})/2 \end{cases} \tag{25}$$

where ζ_{Sc}= 1 indicates that the contact point is located on the lower helical surface of screw, while ζ_{Sc}= −1 indicates that the contact point is on the upper helical surface. ζ_{RSc}= -ζ_{Sc} represents the surface on the roller in contact with the screw.

Similarly, the unit normal vectors of nut and roller satisfy $\boldsymbol{n}_{Nc}$= -$\boldsymbol{n}_{RNc}$. Then, the contact radii and the deflection angle, r_{Nc}, r_{RNc} α_{Nc} and α_{RNc}, are solved by Eq.(26).

$$\begin{cases} \dfrac{l_N\sin\alpha_{Nc}}{2\pi r_{Nc}} + \zeta_{Nc}\cos\alpha_{Nc}\tan\beta_N = \dfrac{l_R\sin\alpha_{RNc}}{2\pi r_{RNc}} - \dfrac{\zeta_{RNc}\cos\alpha_{RNc} r_{RNc}}{\sqrt{r_e^{\,2}-r_{RNc}^{\,2}}} \\ -\dfrac{l_N\cos\alpha_{Nc}}{2\pi r_{Nc}} + \zeta_{Nc}\sin\alpha_{Nc}\tan\beta_N = -\dfrac{l_R\cos\alpha_{RNc}}{2\pi r_{RNc}} - \dfrac{\zeta_{RNc}\sin\alpha_{RNc} r_{RNc}}{\sqrt{r_e^{\,2}-r_{RNc}^{\,2}}} \\ r_{Nc}\sin\alpha_{Nc} = r_{RNc}\sin\alpha_{RNc} \\ r_{Nc}\cos\alpha_{Nc} - r_{RNc}\cos\alpha_{r_{RNc}} = (d_{N0}-d_{R0})/2 \end{cases} \tag{26}$$

where ζ_{RNc}= -ζ_{RSc} and ζ_{Nc}= ζ_{RSc} represent the contact helical surfaces of the nut and roller.

By contacting the screw and nut on both sides of the roller, the rotational motion of the screw is converted into linear thrust of the nut. From the force analysis illustrated in Fig. 2, the force on the thread at the contact point can be decomposed into

$$\begin{cases} Q_{*R} = F_{*R}/(\cos\theta\cos\lambda_R) \\ F_{*Rt} = F_{*R}\tan\lambda_R \\ F_{*Rr} = F_{*R}\tan\theta/\cos\lambda_R \\ F_{*Rr} = F_{*R}\tan\beta_R \end{cases} \quad (* = S, N) \tag{27}$$

where the subscript $*$ ($*=_{S},\ _{N}$) denotes the screw-roller or nut-roller interface, Q_{*R}, F_{*R}, F_{*Rt} and F_{*Rr} represent the normal force, axial force, tangential force and radial force respectively. Therefore, the relationship between the contact angle θ, the helix angle λ_R and flank angle β_R of the roller can be deduced as:

$$\begin{cases} \tan\theta = \tan\beta_R\cos\lambda_R \\ \tan\lambda_R = P_R/\pi d_{R0} \end{cases} \tag{28}$$

2.2.3. Local contact geometry

The material near the initial contact point of the two helical surfaces will deform and expand into an elliptical region after loading, and its semimajor and semiminor axes are a and b respectively, as shown in Fig. 3. The coordinate systems with the contact point as the origin are established within the tangent plane, and the major and minor axis of the contact ellipse are located on the x-axis and y-axis. The principal directions $\boldsymbol{e}_{*1}$ and $\boldsymbol{e}_{*2}$ of the screw or nut determine the x_*-axis and y_*-axis in the o-x_*y_* coordinate system, while the x_{R^*}-axis and y_{R^*}-axis of o-$x_{R^*}y_{R^*}$ are collinear with the principal directions $\boldsymbol{e}_{R^*1}$ and $\boldsymbol{e}_{R^*2}$ of the roller, respectively. The angle between the first principal planes of the two contact surfaces is γ_{R^*}, and $\gamma_{R^*}\in[0,\pi/2]$,which is defined by

$$\gamma_{R*} = \min[\arccos(\boldsymbol{e}_{*1}\cdot\boldsymbol{e}_{R*1}), \pi - \arccos(\boldsymbol{e}_{*1}\cdot\boldsymbol{e}_{R*1})] \quad (*=_{S},_{N}) \tag{29}$$

Then, the surface near the contact point of the screw (or nut) and roller can be expressed as

$$z_* = -\left(\kappa_{*1}x_*^2 + \kappa_{*2}y_*^2\right)/2 \tag{30}$$

$$z_{R*} = \left(\kappa_{R*1}x_{R*}^2 + \kappa_{R*2}y_{R*}^2\right)/2 \tag{31}$$

where κ_{*1} and κ_{*2} are the principal curvatures of the screw or nut, κ_{R^*1} and κ_{R^*2} are the principal curvatures of the roller on the corresponding contact side. The points (x_*, y_*, z_*) and (x_{R^*}, y_{R^*}, z_{R^*}) can be changed into (x, y, z_*) and (x, y, z_{R^*}) by coordinate transformation. Therefore, the distance between these two points before deformation can be expressed as

$$h = z_* - z_{R*} = Ax^2 + By^2 + Cxy \tag{32}$$

$$C = [(\kappa_{*2} - \kappa_{*1})\sin 2\gamma_2 - (\kappa_{R*2} - \kappa_{R*1})\sin 2\gamma_1]/2 \tag{33}$$

where γ_1 is the angle between x-axis and x_{R^*}-axis, γ_2 is the angle between x-axis and x_*-axis. If the local contact geometry satisfies the triangle in Fig. 3 [25], then C= 0. Therefore, based on the law of sines and cosines, there are:

$$\frac{f(\kappa)}{\sin(\pi - 2\gamma_{R*2})} = \frac{\kappa_{*2} - \kappa_{*1}}{2\sin 2\gamma_1} = \frac{\kappa_{R*2} - \kappa_{R*1}}{2\sin 2\gamma_2} \tag{34}$$

$$f(\kappa) = \frac{1}{2}\sqrt{(\kappa_{*2} - \kappa_{*1})^2 + (\kappa_{R*2} - \kappa_{R*1})^2 + 2(\kappa_{*2} - \kappa_{*1})(\kappa_{R*2} - \kappa_{R*1})\cos 2\gamma_{R*}} \tag{35}$$

where $f(\kappa)$ is the function of principal curvatures. From Eq.(36), γ_1 and γ_2 can be obtained by

$$\begin{cases} \gamma_1 = \dfrac{1}{2}\arcsin\{(\kappa_{*2} - \kappa_{*1})\sin 2\gamma_{R*}/[2f(\kappa)]\} \\ \gamma_2 = \dfrac{1}{2}\arcsin\{(\kappa_{R*2} - \kappa_{R*1})\sin 2\gamma_{R*}/[2f(\kappa)]\} \end{cases} \tag{36}$$

In this case, Eq.(32) can be written as h=Ax^2 +By^2, and the relationship between the positive constants A and B is

$$\begin{cases} A + B = (\kappa_{R*2} + \kappa_{R*1} + \kappa_{*2} + \kappa_{*1})/2 = \Sigma\kappa/2 \\ B - A = [(\kappa_{R*2} - \kappa_{R*1})\cos 2\gamma_1 + (\kappa_{*2} - \kappa_{*1})\cos 2\gamma_2]/2 = f(\kappa) \end{cases} \tag{37}$$

Therefore, the coefficients A and B can be obtained by the curvature sum $\Sigma\kappa$ and curvature function $f(\kappa)$, namely,

$$\begin{cases} A = \Sigma\kappa/4 - f(\kappa)/2 \\ B = \Sigma\kappa/4 + f(\kappa)/2 \end{cases} \tag{38}$$

2.2.4. Contact parameters

Based on Hertz contact theory, two contacting helical surfaces will deform under the normal load Q_{*R} ($*=_{S},\ _{N}$), *i.e.*, the points (x, y, z_*) and (x, y, z_{R^*}) will move the displacement u_* and u_{R^*} along the normal direction and overlap with each other. It can be described as

$$u_{R*} + u_* = \delta_H - Ax^2 - By^2 \tag{39}$$

where δ_H is the elastic deformation of two contacts.

Within the contact ellipse $x^2/a^2 + y^2/b^2 = 1$, the contact stress $\sigma(x,y)$ at an arbitrary point (x,y) is

$$\sigma(x,y) = \sigma_H\sqrt{1 - (x/a)^2 - (y/b)^2} \tag{40}$$

where σ_H is the maximum value of contact stress in the contact ellipse, and the contact stress mentioned in the following study refers to σ_H. Based on the force equilibrium conditions, there is $Q_{*R} = \iint\sigma(x,y)\mathrm{d}x\mathrm{d}y$, and after integration σ_H can be expressed as:

$$\sigma_H = 3Q_{*R}/(2\pi ab) \tag{41}$$

Furthermore, the displacement u of the point (x,y) on the surface along the normal direction [25] is

$$u = \left[(1-\nu^2)/(\pi E)\right]\cdot\iint_{\Omega}\sigma(\xi,\eta)\Big/\left[(x-\xi)^2 + (y-\eta)^2\right]^{-1/2}d\xi d\eta \tag{42}$$

where ν and E represent Poisson's ratio and elastic modulus. Similarly, by integrating, there is

$$u = \frac{b\sigma_H(1-\nu^2)}{\pi E}\left[K(e) - \frac{K(e) - L(e)}{e^2}\cdot\frac{x^2}{a^2} - \frac{(e^2-1)K(e) + L(e)}{e^2}\cdot\frac{y^2}{b^2}\right] \tag{43}$$

$$K(e) = \int_0^{\pi/2}\left(1 - e^2\sin^2\varphi\right)^{-1/2}d\varphi \tag{44}$$

$$L(e) = \int_0^{\pi/2}\left(1 - e^2\sin^2\varphi\right)^{1/2}d\varphi \tag{45}$$

where e= $(1\text{-}k_e)^{1/2}$ is the eccentricity of the contact ellipse, and $k_e = b/a$. $K(e)$ and $L(e)$ are complete elliptic integrals of the first and second kinds.

The Poisson's ratio and elastic modulus of the screw or nut are ν_* and E_*, and these of the roller are ν_{R^*} and E_{R^*}, then u_* and u_{R^*} can be obtained from Eq.(43). Substituting them into Eq.(39) gives

$$\frac{b\sigma_H}{E'}\left[K(e) - \frac{K(e) - L(e)}{e^2}\cdot\frac{x^2}{a^2} - \frac{(e^2-1)K(e) + L(e)}{e^2}\cdot\frac{y^2}{b^2}\right] = \delta - Ax^2 - By^2 \tag{46}$$

where $E' = \left[E_R^{-1}(1-\nu_R^2) + E_*^{-1}(1-\nu_*^2)\right]^{-1}$ is the equivalent elastic modulus.

Then, by substituting Eq.(42) into Eq.(47) and comparing the coefficients of the same type at both ends of the equation, the contact parameters are as derived follows:

$$\frac{A}{B} = \frac{(1-e^2)[K(e) - L(e)]}{(e^2-1)K(e) + L(e)} \tag{47}$$

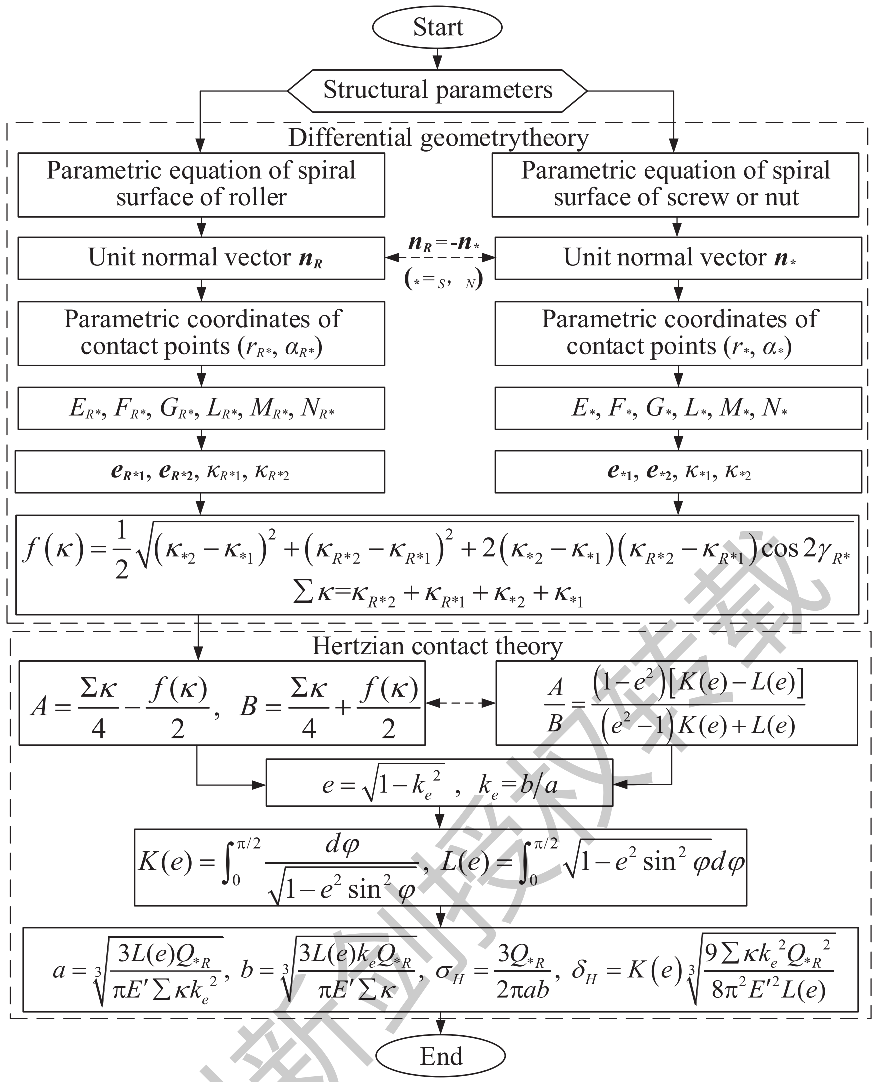

Fig. 4. Flowchart for calculating contact parameters.

$$a=\sqrt[3]{3L(e)Q_{*R}\Big/\left(\pi E'\sum\kappa k_e^2\right)} \tag{48}$$

$$b=\sqrt[3]{3L(e)k_eQ_{*R}\Big/\left(\pi E'\sum\kappa\right)} \tag{49}$$

$$\delta_H=K(e)\sqrt[3]{9\sum\kappa k_e{}^2Q_{*R}{}^2\Big/\left[8\pi^2E'^2L(e)\right]} \tag{50}$$

To sum up, the flowchart for calculating contact parameters is shown in Fig. 4, which can be solved in a parameterized and process-based way.

2.3. 2.3 Numerical example

The structural and material parameters in literature [13] are further used as the numerical example in this paper, and the details are shown in Tables A1 and A2 in the appendix. Under an axial load of 300 N, the lower helical surface $\boldsymbol{\Sigma_{Sl}}$ of the screw is in contact with the upper helical surface $\boldsymbol{\Sigma_{Ru}}$ of the roller, and the lower helical surface $\boldsymbol{\Sigma_{Rl}}$ of the roller is in contact with the upper helical surface $\boldsymbol{\Sigma_{Nu}}$ of the nut. Based on the calculation process shown in Fig. 4, the detailed contact characteristics obtained are listed in Table 1.

The results show the principal curvatures $\kappa_{S1}\cdot\kappa_{S2}<0$ and $\kappa_{N1}\cdot\kappa_{N2}<0$, indicating that the helical surfaces of screw and nut are shaped like saddle surface near the contact point. However, $\kappa_{RS1}\cdot\kappa_{RS2}>0$ and $\kappa_{RN1}\cdot\kappa_{RN2}>0$ indicates that the helical surface of roller is convex near the contact point. Besides, the helical surface of roller is more curved than that of the screw and nut due to its arc-shaped thread profile, resulting in $\kappa_{RS1}>\kappa_{S2}$ and $\kappa_{RN1}>\kappa_{N2}$. Furthermore, the different curvatures, especially $\Sigma\kappa_{SR}>\Sigma\kappa_{NR}$, ultimately contributes to greater contact stress and deformation at the screw-roller interface with a smaller elliptical contact area than those at the nut-roller interface.

In order to visually display the principal directions and contact stress distribution, the contact characteristics are plotted on the spatial tangent planes. As shown in Fig. 5, the x_c-axis is on the line where the axis of the screw or nut points to the axis of the roller. At the contact point of the screw-roller interface, the actual angle between $\boldsymbol{e_{S1}}$ and $\boldsymbol{e_{RS1}}$ is obtuse, therefore the x_S-axis is in the opposite direction of $\boldsymbol{e_{S1}}$ to ensure that $\gamma_{RS}\in[0,\pi/2]$. In addition, the y_S-Axis axis is opposite to $\boldsymbol{e_{S2}}$, thus making the coordinate system o-x_Sy_S a right-handed system, and the y_{RS}-axis, y_{RN}-axis are also specified in this way.

Moreover, Fig. 5 depicts that the contact point between the nut and roller is located on the x_c-axis, its horizontal projection coordinate of is (40, 0), and the contact radii are equal to their nominal radii respectively. However, that coordinate of the contact point between the screw and roller is (24.1193, −1.5662), indicating that there is a certain deflection angle and the contact radii are greater than their nominal radii. The main reason for the above phenomenon is that the screw and

Table 1
Contact characteristics of PRSM (F=300 N).

Contact characteristics	Unit	Screw-roller interface	Nut-roller interface
Principal curvature in the 1st direction	mm^{-1}	$\kappa_{S1} = -3.7845 \times 10^{-4} \kappa_{RS1} = 0.0763$	$\kappa_{N1} = 8.5970 \times 10^{-5} \kappa_{RN1} = 0.0762$
Principal curvature in the 2nd direction	mm^{-1}	$\kappa_{S2} = 0.0298 \kappa_{RS2} = 0.1009$	$\kappa_{N2} = -0.0178 \kappa_{RN2} = 0.1010$
Curvature sum	mm^{-1}	$\Sigma\kappa_{SR} = 0.2067$	$\Sigma\kappa_{NR} = 0.1595$
Contact radius	mm	$r_{Sc} = 24.1710 r_{RSc} = 8.0336$	$r_{Nc} = 40 r_{RNc} = 8$
Contact deflection angle	deg.	$\alpha_{Sc} = -3.6995 \alpha_{RSc} = -11.2727$	$\alpha_{Nc} = 0 \alpha_{RNc} = 0$
Angle between the 1st principal planes	deg.	$\gamma_{RS} = 39.8815$	$\gamma_{RN} = 40.0207$
Angle between x_{RS}-axis, x_{RN}-axis and x-axis	deg.	$\gamma_{RS1} = 17.4733$	$\gamma_{RN1} = 23.9714$
Angle between x_S-axis, x_N-axis and x-axis	deg.	$\gamma_{RS2} = 22.3968$	$\gamma_{RN2} = 16.0493$
Semimajor axis of contact ellipse	mm	$a_{RS} = 0.4201$	$a_{RN} = 0.4584$
Semiminor axis of contact ellipse	mm	$b_{RS} = 0.2143$	$b_{RN} = 0.2335$
Eccentricity of contact ellipse	/	$e_{RS} = 0.8601$	$e_{RN} = 0.8606$
Contact stress	MPa	$\sigma_{HSR} = 2255.8601$	$\sigma_{HNR} = 1897.4493$
Contact deformation	μm	$\delta_{HSR} = 10.1134$	$\delta_{HNR} = 9.2731$

roller with different helix angles are in convex contact, while the nut and roller with equal helix angles are in concave contact with the given parameters.

3. Mathematical modeling of multi-objective optimization

3.1. Design of experiments

The Design of experiments (DOE) method [11] can effectively identify the most sensitive factors to the contact characteristics of the helical surface in PRSM with considering the interaction of all parameters, and then provide the choice of design variables for multi-objective optimization. The flowchart of sensitivity ranking based on DOE is shown in Fig. 6.

The initial input parameters include structural parameters, material properties and axial applied load as shown in Table A1 and Table A2, marked as $\mathbf{x} = (x_1, x_2, \bullet\bullet\bullet, x_i, \bullet\bullet\bullet, x_n)$, $i = 1, 2, \bullet\bullet\bullet, n$, where n represents the total number of input parameters and x_i is the i^{th} parameter. The input parameters are then sampled in the range of $\mathbf{x} \pm 3‰\mathbf{x}$ by Latin hypercube technique [26] with a sampling number of $N = 2000$. Consequently, the sampling vectors are generated, denoted as $\mathbf{x_j} = (x_{1j}, x_{2j}, \bullet\bullet\bullet, x_{ij}, \bullet\bullet\bullet, x_{nj})$, $j = 1, 2, \bullet\bullet\bullet, N$, and x_{ij} is the j^{th} sample of the i^{th} input parameter. Besides, the sampling matrix is recorded as $\mathbf{X} = (\mathbf{x_1}, \mathbf{x_2}, \bullet\bullet\bullet, \mathbf{x_i}, \bullet\bullet\bullet, \mathbf{x_n})$ and $\mathbf{x_i} = (x_{i1}, x_{i2}, \bullet\bullet\bullet, x_{ij}, \bullet\bullet\bullet, x_{iN})^{\mathrm{T}}$ is the sampling vector of x_i.

During the execution of DOE, the responses for each $\mathbf{x_j}$, including the contact position, contact radius, deflection angle, principal curvatures and contact stress, are calculated and recorded as $\mathbf{y_j} = (y_{1j}, y_{2j}, \bullet\bullet\bullet, y_{kj}, \bullet\bullet\bullet, y_{mj})$, $k = 1, 2, \bullet\bullet\bullet, m$, where m is the total number of responses. The matrix for all responses is denoted as $\mathbf{Y} = (\mathbf{y_1}, \mathbf{y_2}, \bullet\bullet\bullet, \mathbf{y_k}, \bullet\bullet\bullet, \mathbf{y_m})$, and $\mathbf{y_k} = (y_{k1}, y_{k2}, \bullet\bullet\bullet, y_{kj}, \bullet\bullet\bullet, y_{kN})^{\mathrm{T}}$ is the sampling vector of the k^{th} response y_k.

The data in the matrices $\mathbf{X}$ and $\mathbf{Y}$ need to be normalized within the range $[-1,1]$ to reduce the influence of orders of magnitude on the analysis, and then the polynomial response surface method is used to fit these data into the mathematical model $\mathbf{y_k} = a_0 + \sum_{i=1}^{n} a_i \mathbf{x_i}$. Finally, the coefficients $A_i = a_i / \sum_{i=1}^{n} a_i$ in the form of percentage, can reflect the contribution of each input parameter to the influence of the k^{th} response and are plotted in an ordered bar graph, namely the Pareto graph.

3.2. 3.2 Sensitivity analysis

The horizontal projection of the contact positions on the screw-roller and nut-roller interfaces of the DOE results is shown in Fig. 7. The blue asterisk represent the contact positions of sampling points and the red dot indicates that of the initial parameters. Fig. 7 shows that the contact positions of sampling points are distributed around the original contact positions and concentrated in a small area, and the contact radius and deflection angle of sampling points have changed.

The Pareto graphs of the top ten parameters most sensitive to the contact characteristics on the screw-roller interface are shown in Fig. 8, where the blue and red bars represent the positive and negative effects respectively.

Fig. 8(a) and (b) depict that β_S contribute most to the deflection angle of the screw and roller, which have negative effect on the roller but positive effect on the screw. Besides, d_{R0}, β_R, P_S and P_R are also sensitive to the deflection angle, but their effects or contributions are somewhat different. In Fig. 8(c) and (d), d_{R0}, β_R and β_S play a major role in the

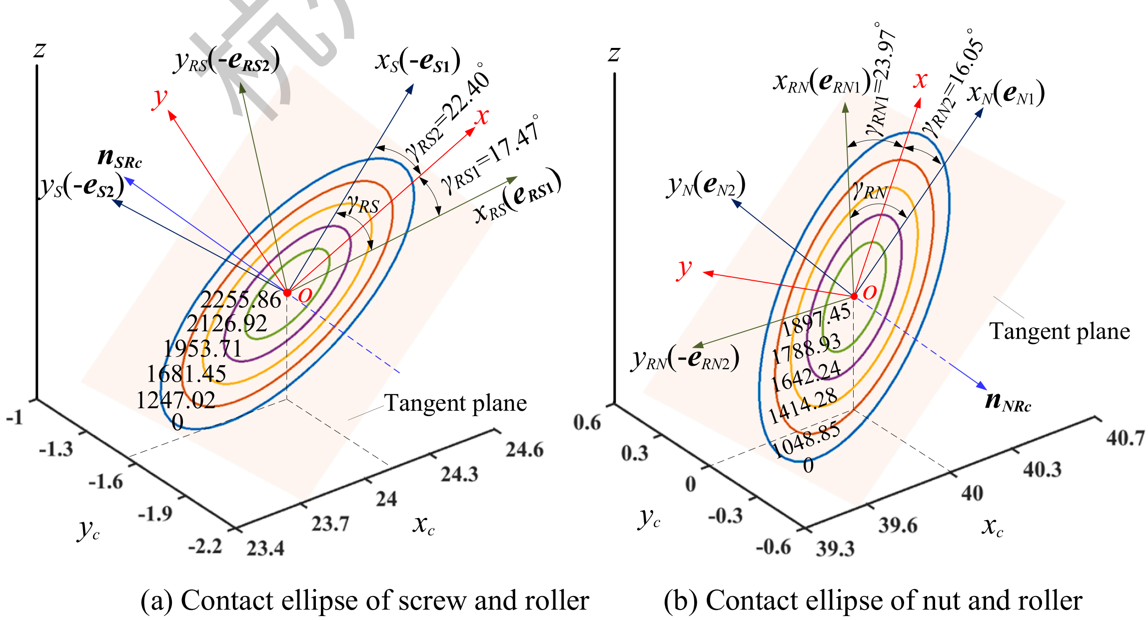

Fig. 5. Principal directions and contact stress distribution.

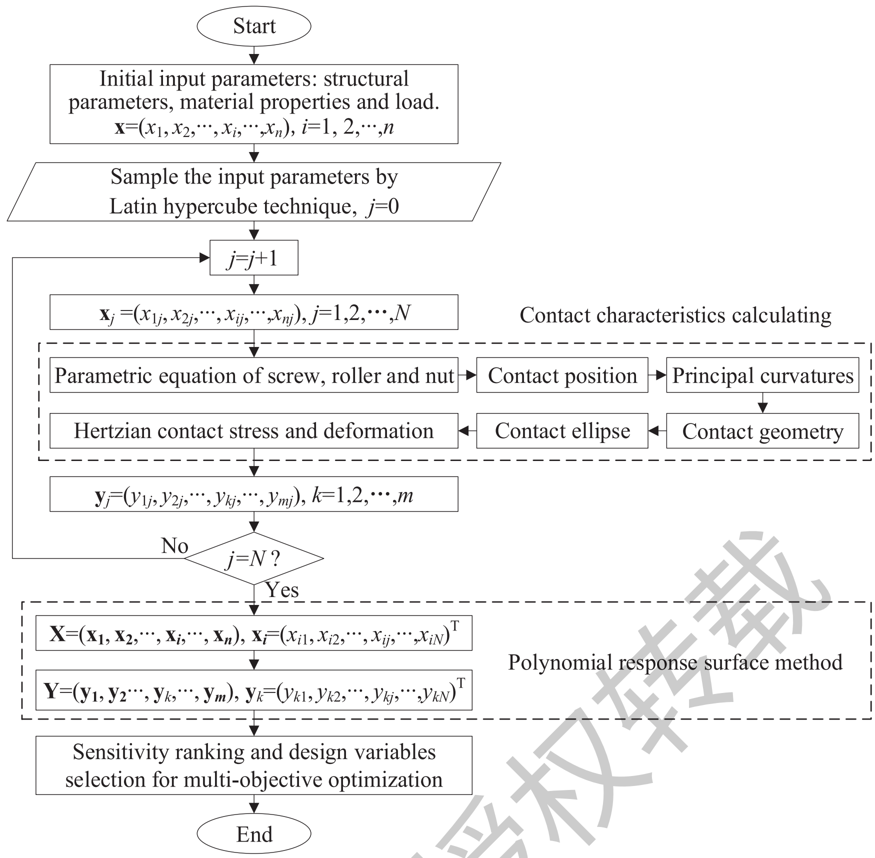

Fig. 6. Flowchart of sensitivity ranking based on DOE.

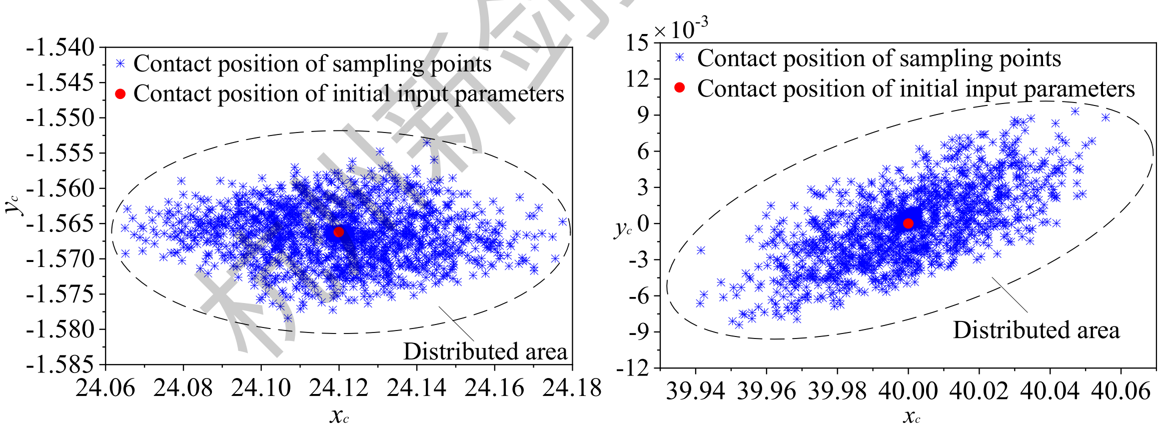

(a) Screw-roller interface (b) Nut-roller interface

Fig. 7. Projection of contact positions of sampling points.

contact radius between the screw and roller, while other parameters have little influence. The effects of d_{R0} and β_S on the screw are negative but positive on the roller, and the effect of β_R is exact converse.

Fig. 8(e) reveals that the negative effect of d_{R0} on the curvature sum $\Sigma\kappa_{SR}$ at the contact point between screw and roller accounts for 50.08%, while β_R and β_S positively contribute 39.23% and 9.00% respectively. Fig. 8(f) shows that β_R has the most significant positive effect on the contact stress σ_{HSR}, followed by d_{R0} with greater negative sensitivity. Then, the positive sensitivity of the applied load F is basically consistent with that of the elastic modulus E_R and E_S. Therefore, a smaller contact stress can be obtained by reducing the applied load and elastic modulus based on Hertz contact theory. Furthermore, Poisson's ratio ν_S and ν_R rank after β_S, and they have a positive impact on σ_{HSR}.

Similarly, the Pareto graphs for the contact characteristics on the nut-roller interface are shown in Fig. 9. It can be concluded from Fig. 9 (a) and (b) that the most sensitive parameters to the deflection angle of roller and nut are P_N, P_R, d_{R0}, β_R and β_N in sequence, in which P_N, d_{R0} and β_N have positive effects, while P_R and β_R have negative effects. Fig. 9(c) and (d) depict that d_{R0}, β_N and β_R are the main contributors to the contact radius of roller and nut, and d_{R0}, β_N and P_N are positive effects and the other two are negative effects. Notably, the influence of structural parameters on the contact position of nut and roller is almost the same, which is mainly caused by their concave meshing and equal helix angle.

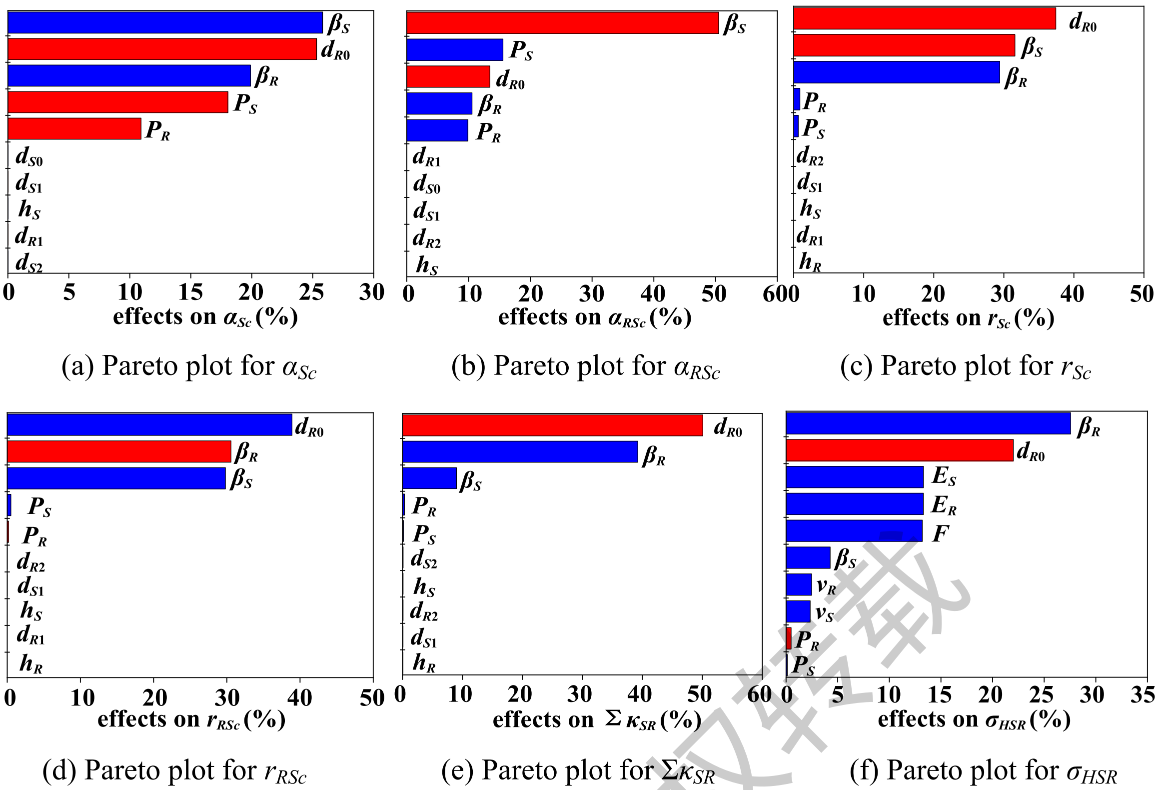

(a) Pareto plot for α_{Sc} (b) Pareto plot for α_{RSc} (c) Pareto plot for r_{Sc}

(d) Pareto plot for r_{RSc} (e) Pareto plot for $\Sigma\kappa_{SR}$ (f) Pareto plot for σ_{HSR}

Fig. 8. Pareto graphs for the contact characteristics on the screw-roller interface.

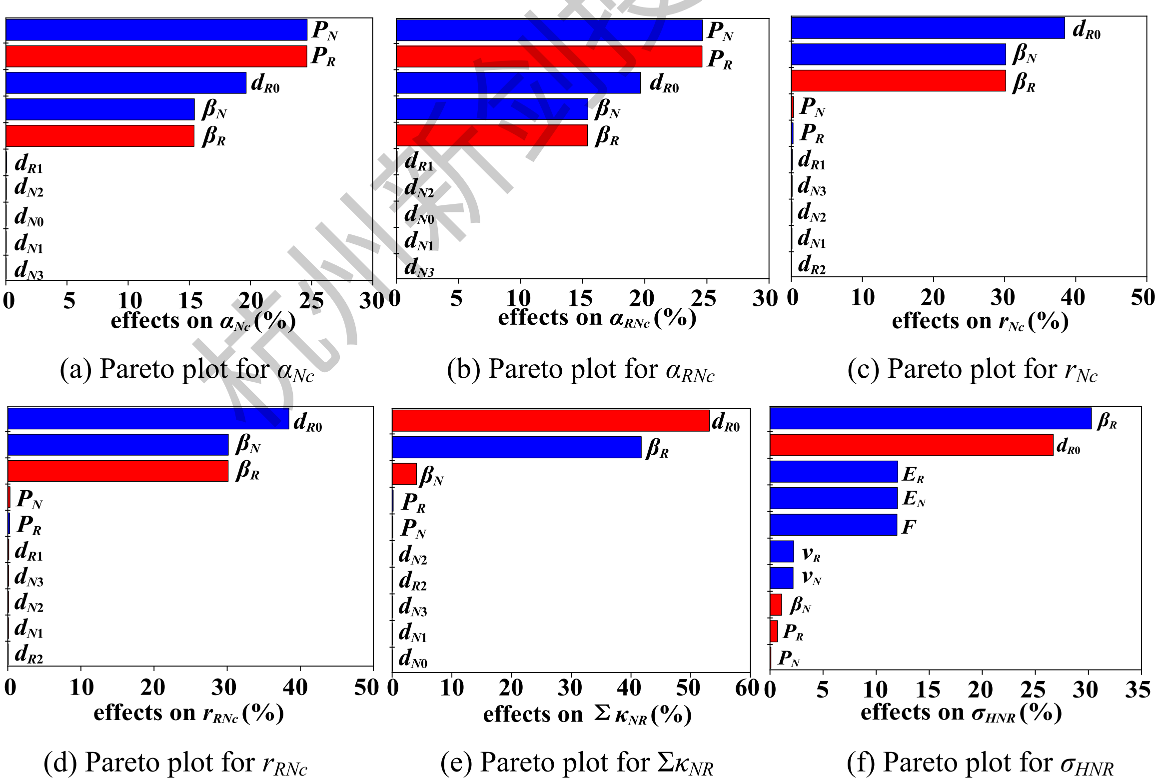

(a) Pareto plot for α_{Nc} (b) Pareto plot for α_{RNc} (c) Pareto plot for r_{Nc}

(d) Pareto plot for r_{RNc} (e) Pareto plot for $\Sigma\kappa_{NR}$ (f) Pareto plot for σ_{HNR}

Fig. 9. Pareto graphs for the contact characteristics on the nut-roller interface.

Fig. 9(e) demonstrates that d_{R0} and β_R account for 53.13% and 41.72% of the negative effects on the curvature sum $\Sigma\kappa_{NR}$, respectively, and β_N accounts for 4.07% of the positive effects. The parameters shown in Fig. 9(f) affect the contact stress between the nut and roller in the way similar to that in Fig. 8(f).

In conclusion, the nominal diameter of roller d_{R0}, the pitches P_S, P_R, P_N and flank angles β_S, β_R, β_N are sensitive to the contact radius and deflection angle, because they mainly determine the properties of helical

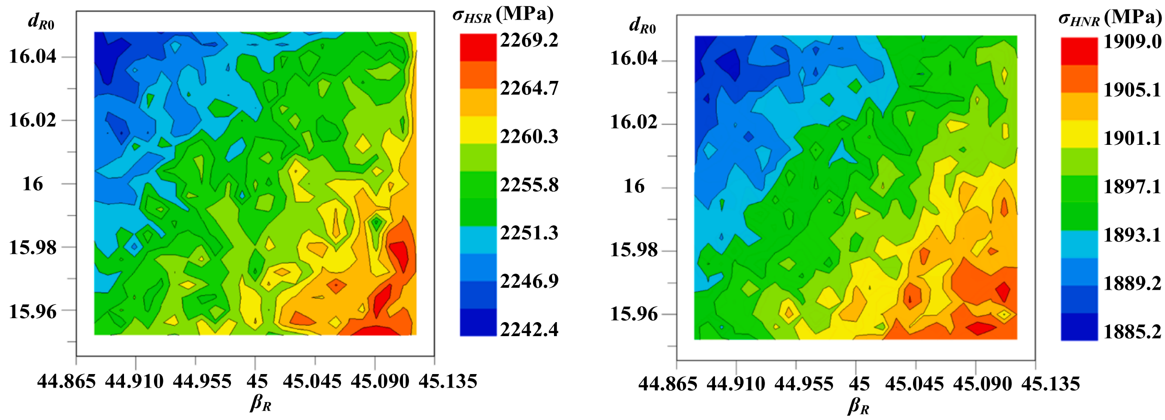

(a) Screw-roller interface (b) Nut-roller interface

Fig. 10. Contour map of contact stress affected by d_{R0} and β_R.

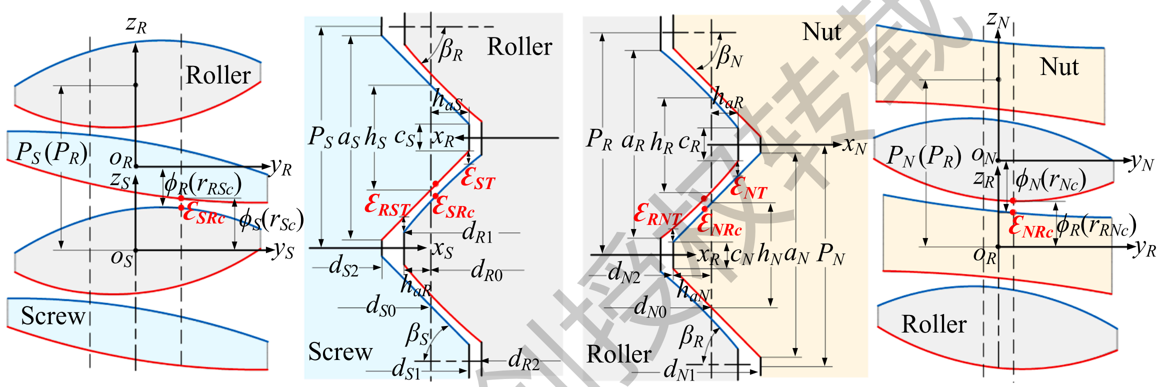

Fig. 11. Geometric constraints in PRSM.

surfaces. Due to the difference between concave and convex contact, the contributions and effects of the above parameters on the nut and roller are almost identical, but the most sensitive parameter has opposite effect on the screw and roller.

The contour maps of contact stress affected by d_{R0} and β_R based on DOE results are shown in Fig. 10. Obviously, the larger d_{R0} and the smaller β_R results in the lower contact stress, because it causes the larger radius of the arc thread profile of the roller, *i.e.*, the less curved with smaller curvature sum. Meanwhile, by decreasing β_R can also reduce the normal force acting on the contact point under a given load.

3.3. Constraint conditions

The multi-objective optimization of PRSM is carried out to obtain the smaller contact stress of screw-roller and nut-roller interfaces simultaneously. In order not to change the dimensions and transmission ratio of PRSM, the flank angles β_S, β_R and β_N are selected as the design variables, denoted as $\boldsymbol{\beta} = (\beta_S, \beta_R, \beta_N)$. The nominal diameter of roller d_{R0} and other parameters are taken as the design constants, denoted as $\mathbf{C_X}$. Then, the contact stress can be regarded the high-dimensional and multi-order nonlinear implicit objective function determined by $\boldsymbol{\beta}$ and $\mathbf{C_X}$, and expressed as $\sigma_{HSR} = g_{SR}(\boldsymbol{\beta}, \mathbf{C_X})$ and $\sigma_{HNR} = g_{NR}(\boldsymbol{\beta}, \mathbf{C_X})$. Moreover, the geometric constraint conditions are proposed to avoid such phenomena as thread overlap or stress concentration in the optimized PRSM, as shown in Fig. 11.

Firstly, the threads of screw, roller and nut should avoid sharpened crown or intersecting bottom, and the constraints are

$$\begin{cases} P_S - a_S > 0 \\ c_S > 0 \end{cases}, \begin{cases} P_S - a_S > 0 \\ c_S > 0 \end{cases} \text{ and } \begin{cases} P_N - a_N > 0 \\ c_N > 0 \end{cases} \tag{51}$$

where a_S, a_R and a_N are the root widths, and c_S, c_R and c_N are the crest widths, and can be calculated as

$$\begin{cases} a_S = h_S + (d_{S0} - d_{S2})\tan\beta_S \\ c_S = h_S - (d_{S0} - d_{S1})\tan\beta_S \end{cases} \tag{52}$$

$$\begin{cases} a_R = h_R + \sqrt{4r_e^2 - d_{R2}^2} - d_{R0}\cot\beta_R \\ c_R = h_R + \sqrt{4r_e^2 - d_{R1}^2} - d_{R0}\cot\beta_R \end{cases} \tag{53}$$

$$\begin{cases} a_N = h_N + (d_{N1} - d_{N0})\tan\beta_N \\ c_N = h_N - (d_{N0} - d_{N2})\tan\beta_N \end{cases} \tag{54}$$

Secondly, the thread of the roller should be avoided overlapping with the thread of the screw or nut. By substituting the coordinates of the contact point into the corresponding parametric equation, the axial clearance ε_{SRc} or ε_{NRc} between the thread surfaces to be contacted can be deduced as

$$\begin{cases} \varepsilon_{SRc} = \phi_S(r_{Sc}) + \alpha_{Sc} l_S/2\pi + \phi_R(r_{RSc}) + \alpha_{RSc} l_R/2\pi - P_R/2 \\ \varepsilon_{NRc} = \phi_N(r_{Nc}) + \alpha_{Nc} l_N/2\pi + \phi_R(r_{RNc}) + \alpha_{RNc} l_R/2\pi - P_R/2 \end{cases} \tag{55}$$

Therefore, the constraint conditions for non-interference of threads in PRSM are

$$\varepsilon_{SRc} > 0 \text{ and } \varepsilon_{NRc} > 0 \tag{56}$$

Thirdly, the stress concentration caused by the contact at the crown of the threads should also be avoided. Referring to Fig. 11, the axial

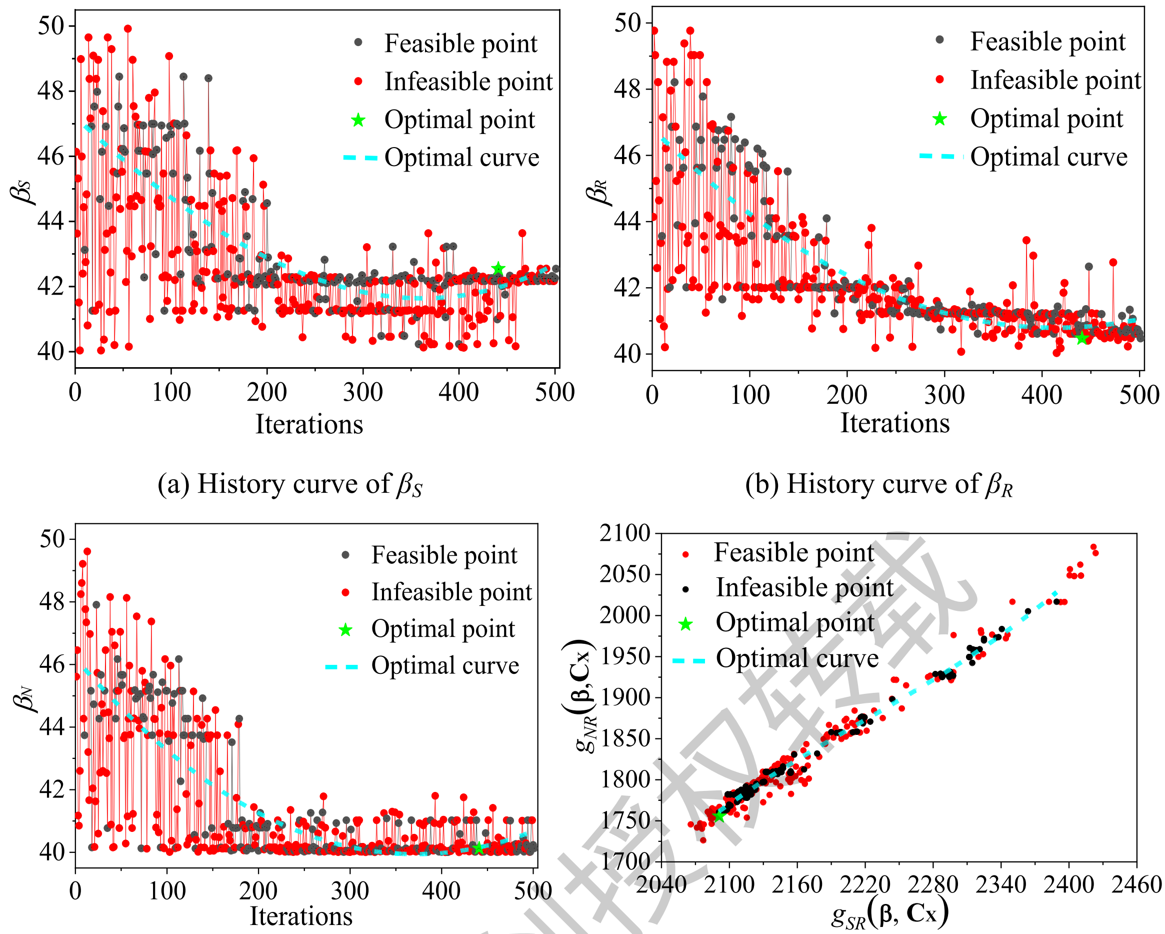

(a) History curve of β_S (b) History curve of β_R

(c) History curve of β_N (d) Scatter plot of objective functions

Fig. 12. Multi-objective optimization history graphs of contact stress based on NSGA-II algorithm.

Table 2
Comparison of initial and optimal contact characteristics (F=300 N).

Parameters	Unit	Initial	Optimum	Rate (-%)
β_S	deg.	45	42.5388	5.4694
β_R	deg.	45	40.4725	10.0612
β_N	deg.	45	40.1249	10.8335
Q_{SR}, Q_{NR}	N	425.3123	395.4916	7.0115
$\Sigma\kappa_{SR}$	mm^{-1}	0.2067	0.1911	7.5116
$\Sigma\kappa_{NR}$	mm^{-1}	0.1595	0.1464	8.1786
$g_{SR}(\beta, C_X)$	MPa	2255.8601	2087.8859	7.4461
$g_{NR}(\beta, C_X)$	MPa	1897.4493	1744.8579	8.0419
δ_{HSR}	μm	10.1134	9.3779	7.2721
δ_{HNR}	μm	9.2731	8.5642	7.6441
(r_{Sc}, α_{Sc})	(mm, deg.)	(24.1710, −3.6995)	(23.8722, −4.1559)	–
(r_{RSc}, α_{RSc})	(mm, deg.)	(8.0336, −11.2727)	(8.3843, −11.8005)	–
(r_{Nc}, α_{Nc})	(mm, deg.)	(40, 0)	(39.9948, −0.0090)	–
(r_{RNc}, α_{RNc})	(mm, deg.)	(8, 0)	(7.9434, −0.0242)	–

clearance from the thread crown of screw or nut to the corresponding helical surface of roller, denoted as ε_{ST} or ε_{NT}, can be derived as

$$\begin{cases} \varepsilon_{ST} = \phi_R(d_{R0}/2 - h_{aS}) - c_S/2 \\ \varepsilon_{NT} = \phi_R(d_{R0}/2 - h_{aN}) - c_N/2 \end{cases} \tag{57}$$

where h_{aS} and h_{aN} are the thread addendum of the screw and nut respectively.

Similarly, the axial clearance ε_{RST} or ε_{RNT}, from the thread crown of roller to the corresponding helical surface of screw or nut, can be expressed as

$$\begin{cases} \varepsilon_{RST} = (P_R - c_R - h_S)/2 - h_{aR}\tan\beta_S \\ \varepsilon_{RNT} = (P_R - c_R - h_N)/2 - h_{aR}\tan\beta_N \end{cases} \tag{58}$$

where h_{aR} is the thread addendum of the roller. Additionally, h_{aS}, h_{aR} and h_{aN} are given by

$$\begin{cases} h_{aS} = (d_{S1} - d_{S0})/2 \\ h_{aR} = (d_{R1} - d_{R0})/2 \\ h_{aN} = (d_{N0} - d_{N2})/2 \end{cases} \tag{59}$$

In summary, the constraints for avoiding stress concentration are

$$\begin{cases} \varepsilon_{RST} > \varepsilon_{SRc} \\ \varepsilon_{ST} > \varepsilon_{SRc} \end{cases} and \begin{cases} \varepsilon_{RNT} > \varepsilon_{NRc} \\ \varepsilon_{NT} > \varepsilon_{NRc} \end{cases} \tag{60}$$

Based on the above strong constraints, the mathematical model for multi-objective optimization on the contact stress of screw-roller and nut-roller interface can be expressed as

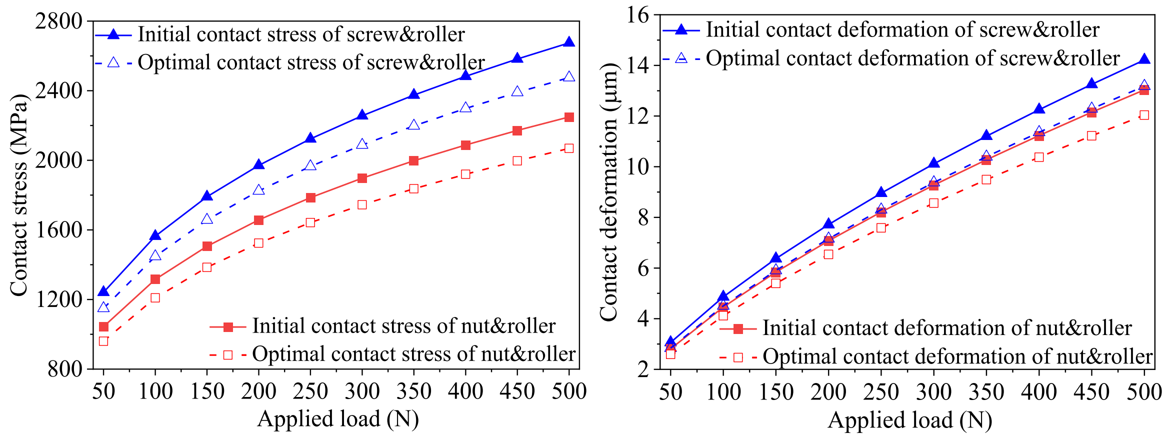

(a) Contact stress (b) Contact deformation

Fig. 13. Contact stress and deformation on helical surfaces after structural design.

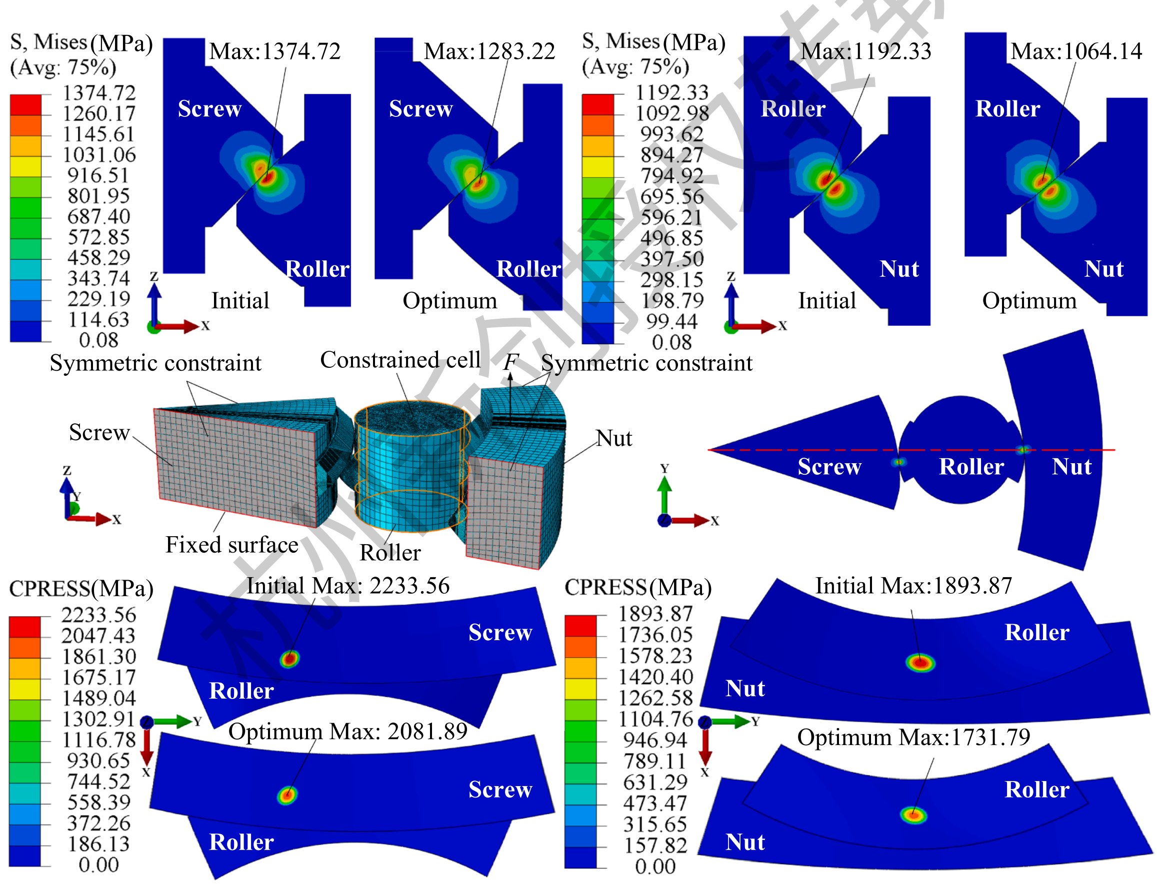

Fig. 14. Comparison of the contact characteristics between the initial and optimized PRSM by FEM.

$$
\begin{gathered}
\mathit{find}\ \boldsymbol{\beta}=(\beta_S,\beta_R,\beta_N) \\
\min\ \sigma_{HSR}=g_{SR}(\boldsymbol{\beta},\mathbf{C_X})\&\sigma_{HNR}=g_{NR}(\boldsymbol{\beta},\mathbf{C_X}) \\
\text{s.t.}\ \left\{ \begin{array}{l} a_S-P_S<0;a_R-P_R<0;a_N-P_N<0;\ -c_S<0;-c_R<0;-c_N<0;\ -\varepsilon_{SRc}<0;-\varepsilon_{NRc}<0; \\ \varepsilon_{SRc}-\varepsilon_{RST}<0;\varepsilon_{NRc}-\varepsilon_{RNT}<0;\varepsilon_{SRc}-\varepsilon_{ST}<0;\varepsilon_{NRc}-\varepsilon_{NT}<0;\boldsymbol{\beta}^l\le\boldsymbol{\beta}\le\boldsymbol{\beta}^u \end{array} \right.
\end{gathered}
\tag{61}
$$

where $\boldsymbol{\beta}^l$ and $\boldsymbol{\beta}^u$ are the lower and upper limit of the design space respectively.

4. Results and discussion

4.1. Optimization results

In the design space of [40°, 50°] considering transmission efficiency [8], the multi-objective optimization of contact stress of PRSM is carried out based on NSGA-II algorithm [13], in which the maximum generation and population size are 25 and 20. The history graphs with 501 iterations in total are shown in Fig. 12, and each iteration is calculated by the parameterized program. The infeasible points indicated in red are those that do not meet the constraint conditions in the optimization process. On the contrary, the feasible points are displayed in black, and the one that minimizes the values of the two objective functions is the optimal point and is represented by a green pentagram. The optimal curve is shown by the fitted blue dash line.

The comparison of initial and optimal contact characteristics under the axial load of 300 N is shown in Table 2. After optimization, the flank angles of screw, roller and nut are reduced by 5.47%, 10.06% and 10.83% respectively, and the normal forces Q_{SR} and Q_{NR} are reduced by 7.01% without changing the applied load. At the contact points of screw-roller and nut-roller interfaces, the curvature sum decreases by 7.51% and 8.18%, the corresponding contact stress decreases by 7.45% and 8.04%, and the contact deformation also decreases by 7.27% and 7.64%, respectively. Additionally, the contact point between the screw and roller is closer to the axis of the screw while away from the roller, and the deflection angles of the two increase in the optimized PRSM. The contact point between the nut and roller deviates slightly from its initial position and is no longer on their nominal diameters.

After the structural design of PRSM, the contact stress and deformation of the corresponding two helical surfaces under different applied loads are further shown in Fig. 13. Compared with the initial structure, the optimal design can effectively reduce the contact stress and deformation of the threads. Importantly, with the increasing sophistication of precision grinding technology [27], the structurally optimized PRSM can be manufactured by redesigning the corresponding grinding wheel profiles.

4.2. Verification

The finite element (FE) model of PRSM with the parameters of the numerical example is established in ABAQUS 6.14 to verify the validity of the mathematical model. As shown in Fig. 14, both the screw and nut are simplified to 1/10 sector portion of the overall structure with one thread, and the thread of roller only retain the contact parts. The linear hexahedral element type C3D8R is used to mesh the FE model, and the contact thread surfaces are further refined to reduce the calculation cost while ensuring the accuracy. After the grid independence test and convergence analysis, the global and local mesh sizes are set as 0.8 mm and 0.035 mm respectively, including 1723,991 nodes and 1599,652 elements in total.

Furthermore, the coordinates and contact surfaces of the screw, roller and nut are consistent with the numerical example. Both sides of the screw and the nut are symmetrically constrained, and the bottom surface of the screw is fixed with six degrees of freedom. Meanwhile, only the freedom on the z-axis of the screw, roller and nut is released. On the nut-roller interface, the master surface is assigned to the nut and the slave surface to the roller, while on the screw-roller interface, the master surface is assigned to the roller and the slave surface to the screw. Moreover, the interaction and contact properties for the standard surface-to-surface contacts are set as small sliding with a friction coefficient of 0.2. To successfully establish the contact relationships, two static general steps are created. A small axial displacement of 0.5 mm is firstly applied on the nut to eliminate the clearance between the threads, and then replaced by an axial force of 300 N in the second step. The FE model of the optimized PRSM is also established in this way, and the comparison of FEM results is shown in Fig. 14.

The xz view in Fig. 14 shows that the maximum von Mises stress is concentrated at a certain depth below the contact surface of the three parts and there is almost no stress distribution in the rest. Therefore, threads are more prone to plastic deformation or fatigue failure in PRSM. The von Mises stress nephogram in xy view clearly shows that the contact point between the nut and roller is basically located on the connecting line of their axis, while the contact point between the screw and roller is below that line.

The maximum von Mises stress on the two contact sides of the roller decreased by 6.66% and 10.75% from the initial 1374.72 MPa and 1192.23 MPa after optimization. Meanwhile, the initial contact stresses of the screw-roller and nut-roller interfaces are 2233.56 MPa and 1893.87 MPa, which are reduced to 2081.89 MPa and 1731.79 MPa of the optimized PRSM, respectively. The above data show that these stresses can be effectively reduced through the structural optimization design of PRSM.

Noteworthy, by comparing the contact stress, contact radius and deflection angle shown in Fig. 14 and Table 2, it can be found that the relative errors of the results obtained by the analytical method and FEM are all less than 1%. Besides, some additional numerical examples are performed, and the results are shown in Table A3 and A4 in the appendix. By comparing the results with the FEM solutions and published data, it shows that the relative errors are within the acceptable range, which fully verifies the validity of the mathematical model. Therefore, the proposed contact model can be used to calculate the contact characteristics of PRSM with the change of parameters, especially in the iterative process of structural optimization design.

5. Conclusions

In this paper, the contact characteristics of PRSM are systematically and comprehensively studied based on the developed contact modeling. A process-based parameterization method is proposed to accurately calculate the contact characteristics with arbitrary parameter changes, which is further used for multi-objective optimization to achieve the structural design. The mathematical model is well verified by FEM and the published data.

The results show that among the structural parameters of PRSM, the nominal diameter of roller d_{R0}, the pitches P_S, P_R, P_N and flank angles β_S, β_R, β_N have great influence on the corresponding contact characteristics, especially β_R and d_{R0} contributes significantly to the contact radius, curvature sum and contact stress. The sensitivity of these parameters to the nut and roller is basically the same, but the most sensitivity parameter affects the screw and roller in the opposite way. Under the proposed constraints of avoiding crown sharpening, bottom intersection, thread overlap and stress concentration, the structural optimization design of PRSM with flank angles as the design variables can effectively reduce the contact stress and contact deformation of both screw-roller and nut-roller interfaces. The contact model proposed in this paper is universal, and the research results are of great significance to improve the contact performance of the transmission thread pairs.

CRediT authorship contribution statement

Qin Yao: Writing – original draft, Conceptualization, Software, Validation. **Mengchuang Zhang:** Supervision, Methodology, Writing – review & editing. **Shangjun Ma:** Writing – review & editing.

Declaration of Competing Interest

The authors declare that they have no known competing financial interests or personal relationships that could have appeared to influence the work reported in this paper.

Acknowledgments

This work was supported in part by the National Natural Science Foundation of China (grant no. 51875458), Industrial Development and Foster Project of Yangtze River Delta Research Institute of NPU, Taicang, China (grant no. CY20210201).

Appendix

See Appendix Tables A1–A4.

Table A1
Structural parameters of PRSM.

Parameters	Unit	Screw		Roller		Nut	
		Symbol	Value	Symbol	Value	Symbol	Value
Nominal diameter	mm	d_{S0}	48	d_{R0}	16	d_{N0}	80
Major diameter	mm	d_{S1}	49.43	d_{R1}	17.6	d_{N1}	82.62
Minor diameter	mm	d_{S2}	45.38	d_{R2}	14	d_{N2}	78.57
Thread thickness	mm	h_S	2	h_R	2.4	h_N	2
Pitch	mm	P_S	5	P_R	5	P_N	5
Flank angle	deg.	β_S	45	β_R	45	β_N	45
Starts of thread	–	n_S	5	n_R	1	n_N	5
External diameter	mm	–	–	–	–	d_{N3}	100

Table A2
Material properties of PRSM.

Random variables	Unit	Symbol	Value
Elastic modulus	MPa	E_S, E_R, E_N	212000
Poisson's ratio	–	ν_S, ν_R, ν_N	0.29
Yield limit	MPa	σ_s	1617
Contact fatigue limit	MPa	σ_{Hlim}	2450

Table A3
Contact characteristics with arbitrary structural parameters (F=200 N, elastic modulus 212000 MPa, Poisson's ratio 0.29).

Structural parameters	Nominal diameter (mm)	Flank angle (deg.)	Number of starts		Pitch (mm)
Screw	48	43.2871	5		4.9999
Roller	16	42.0761	1		5.0012
Nut	80	42.6413	5		5.0004
Contact pair (FE model in this paper)		Contact characteristics	Analytical solution	FEMsolution	Relative error
Screw-roller interface		Contact radius (mm)	24.0040	24.0208	0.07%
			8.2301	8.2359	0.07%
		Contact deflection angle (deg.)	-4.0247	-4.0408	0.40%
			-11.6859	-11.6373	0.42%
		Contact stress (MPa)	1874.8247	1840.6982	1.85%
Nut-roller interface		Contact radius (mm)	40.0840	40.0897	0.01%
			8.0871	8.0774	0.12%
		Contact deflection angle (deg.)	-0.0121	-0.0139	0.0018
			0.0242	0.0299	0.0057
		Contact stress (MPa)	1570.4866	1556.3491	0.91%

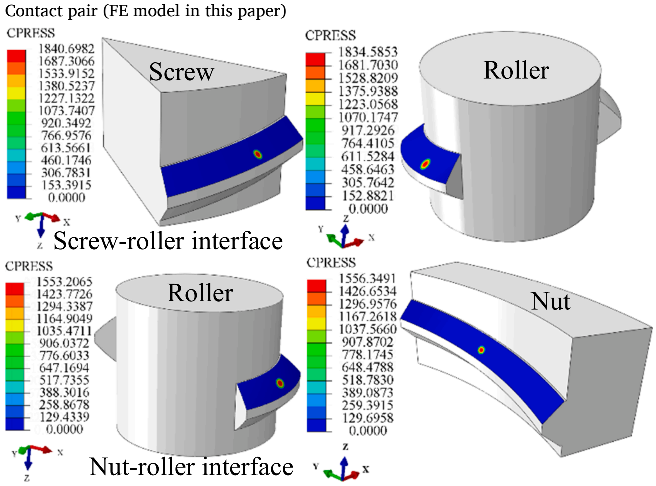

Table A4
Numerical example in Ref.[21] for validation of the contact model in this paper (F=200 N, elastic modulus 212000 MPa, Poisson's ratio 0.29).

Structural parameters	Nominal radius (mm)	Flank angle (deg.)	Number of starts	Pitch (mm)
Screw	9.75	45	5	2
Roller	3.25	45	1	2
Nut	16.25	45	5	2
Contact pair (Ideal elastic FE model in Ref.[21])	Contact characteristics	Analytical solution	Ref.[21]	Relative error

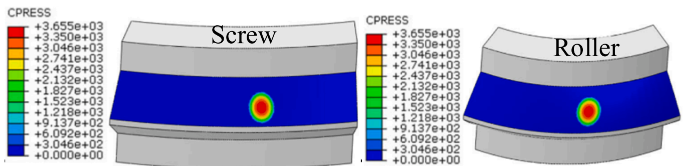

Nut-roller interface

	Contact radius (mm)	9.8118	9.8173	0.06%
		3.2598	3.2635	0.11%
	Contact deflection angle	3.6588	3.6605	0.05%
	(deg.)	11.6010	11.7030	0.87%
	Contact stress (MPa)	3592.8289	3655	1.70%

Nut-roller interface

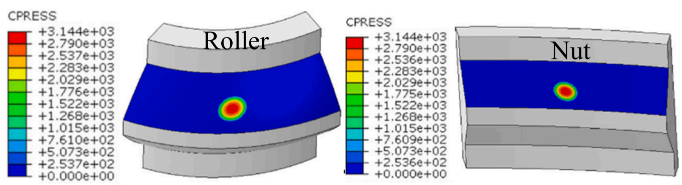

	Contact radius (mm)	16.25	16.25	0
		3.25	3.25	0
	Contact deflection angle	0	0	0
	(deg.)	0	0	0
	Contact stress (MPa)	3037.1383	3144	3.39%

References

[1] Zheng S, Fu Y, Wang D, Zhang W, Pan J. Investigations on system integration method and dynamic performance of electromechanical actuator. Sci Prog 2020;103(3):0036850420940923. https://doi.org/10.1177/0036850420940923.

[2] Arriola D, Thielecke F. Model-based design and experimental verification of a monitoring concept for an active-active electromechanical aileron actuation system. Mech Syst Signal Process 2017;94:322–45. https://doi.org/10.1016/j.ymssp.2017.02.039.

[3] Mamaev I, Morozov VV, Fedotov OV, Filimonov V. Precision of a roller screw actuator transmission for a radio telescope. Russ Eng Res 2015;35(12):919–23. https://doi.org/10.3103/S1068798X15120102.

[4] Yang X, Yan M, Zhou Y, Liu R. The dynamic analysis of planetary roller screw in tree-climbing robot. J Phys: Conf Ser 2021;2029(1):012060. https://doi.org/10.1088/1742-6596/2029/1/012060.

[5] Guadagno M, Loss J, Pearce J. Open source 3D-printable planetary roller screw for food processing applications. Technologies 2021;9(2):24. https://doi.org/10.3390/technologies9020024.

[6] Xie Z, Xue Q, Wu J, Gu L, Wang L, Song B. Mixed-lubrication analysis of planetary roller screw. Tribol Int 2019;140:105883. https://doi.org/10.1016/j.triboint.2019.105883.

[7] Zhou G, Zhang Y, Wang Z, Pu W. Analysis of transient mixed elastohydrodynamic lubrication in planetary roller screw mechanism. Tribol Int 2021;163:107158. https://doi.org/10.1016/j.triboint.2021.107158.

[8] Qiao G., Liu G., Ma S., Shi Z., and Lim TC. Friction Torque Modelling and Efficiency Analysis of the Preloaded Inverted Planetary Roller Screw Mechanism. ASME International Design Engineering Technical Conferences and Computers and Information in Engineering Conference. 2017. Cleveland, Ohio, USA. https://doi.org/10.1115/detc2017–68006.

[9] Qiao G, Liu G, Ma S, Shi Z, Wang Y, Lim TC. An improved thermal estimation model of the inverted planetary roller screw mechanism. Proc Inst Mech Eng Part C- J Mech Eng Sci 2018;232(23):4430–46. https://doi.org/10.1177/0954406218762961.

[10] Aurégan G, Fridrici V, Kapsa P, Rodrigues F. Wear behavior of martensitic stainless steel in rolling-sliding contact for planetary roller screw mechanism: study of the WC/C solution. Tribol Online 2016;11(2):209–17. https://doi.org/10.2474/trol.11.209.

[11] Yao Q, Liu Y, Zhang M, Liu G, Ma S. Investigation on the uncertain factors of the elastic–plastic contact characteristics of the planetary roller screw mechanism. Proc Inst Mech Eng Part C- J Mech Eng Sci 2019;233(5):1795–806. https://doi.org/10.1177/0954406218772607.

[12] Du X, Chen B, Zheng Z. Investigation on mechanical behavior of planetary roller screw mechanism with the effects of external loads and machining errors. Tribol Int 2021;154:106689. https://doi.org/10.1016/j.triboint.2020.106689.

[13] Yao Q, Zhang M, Liu Y, Ma S. Multi-objective optimization of planetary roller screw mechanism based on improved mathematical modelling. Tribol Int 2021;161:107095. https://doi.org/10.1016/j.triboint.2021.107095.

[14] Fu X, Liu G, Ma S, Tong R, Lim TC. A comprehensive contact analysis of planetary roller screw mechanism. J Mech Des 2016;139(1):012302–1-012302-11. https://doi.org/10.1115/1.4034580.

[15] Liu Y, Shang Y, Wang J. Mathematical analysis of the meshing performance of planetary roller screws applying different roller thread shapes. Adv Mech Eng 2017;9(5):1–11. https://doi.org/10.1177/1687814017703009.

[16] Sandu S, Biboulet N, Nelias D, Abevi F. Analytical prediction of the geometry of contact ellipses and kinematics in a roller screw versus experimental results. Mech Mach Theory 2019;131:115–36. https://doi.org/10.1016/j.mechmachtheory.2018.09.013.

[17] Liu Y, Wang J, Cheng H, Sun Y. Kinematics analysis of the roller screw based on the accuracy of meshing point calculation. Math Probl Eng 2015;2015:10. https://doi.org/10.1155/2015/303972.

[18] Fu X, Liu G, Ma S, Tong R, Li X. An efficient method for the dynamic analysis of planetary roller screw mechanism. Mech Mach Theory 2020;150:103851. https://doi.org/10.1016/j.mechmachtheory.2020.103851.

[19] Jones MH, Velinsky SA. Contact kinematics in the roller screw mechanism. J Mech Des 2013;135(5):051003. https://doi.org/10.1115/1.4023964.

[20] Sandu S, Biboulet N, Nelias D, Abevi F. An efficient method for analyzing the roller screw thread geometry. Mech Mach Theory 2018;126:243–64. https://doi.org/10.1016/j.mechmachtheory.2018.04.004.

[21] Ma S, Wu L, Liu G, Fu X. Local contact characteristics of threaded surfaces in a planetary roller screw mechanism. Mech Based Des Struct 2020;48(1):1–26. https://doi.org/10.1080/15397734.2019.1615944.

[22] Ma S, Wu L, Fu X, Li Y, Liu G. Modelling of static contact with friction of threaded surfaces in a planetary roller screw mechanism. Mech Mach Theory 2019;139:212–36. https://doi.org/10.1016/j.mechmachtheory.2019.04.014.

[23] Abevi F, Daidie A, Chaussumier M, Orieux S. Static analysis of an inverted planetary roller screw mechanism. J Mech Robot 2016;8(4):041020–041020-14. https://doi.org/10.1115/1.4033159.

[24] Ciarlet PG, Li TT. Differential Geometry: Theory and Applications. Higher Education Press; 2008.

[25] Johnson KL. Contact Mechanics. Cambridge University Press; 1987.

[26] Shu Z, Jirutitijaroen P. Latin hypercube sampling techniques for power systems reliability analysis with renewable energy sources. IEEE T Power Syst 2011;26(4):2066–73. https://doi.org/10.1109/TPWRS.2011.2113380.

[27] Guo B, Meng Q, Wu G, Zhao Q, Li S. Parallel axis precision grinding of micro-tooth internal thread with the coarse-grains CBN wheels. J Manuf Process 2022;74:474–85. https://doi.org/10.1016/j.jmapro.2021.12.042.